

Random First Order Transition theory for glassy dynamics in a cellular Potts model for biological tissues

Souvik Sadhukhan^{*} and Saroj Kumar Nandi[†]

TIFR Centre for Interdisciplinary Sciences, Tata Institute of Fundamental Research, Hyderabad - 500046, India

Simulation studies of vertex models have argued glassiness in confluent cellular systems is controlled by a rigidity transition and the observed shape index has been interpreted as a structural order parameter for glass transition. We show that such an interpretation is incorrect. Moreover, effect of arbitrary cell boundaries and nature of T_1 transitions in such simulations remain unclear. We combine numerical simulations of a more microscopic, cellular Potts model and analytical study based on random first order transition (RFOT) theory of glass to develop a coherent theoretical framework for a confluent system showing that glassiness is controlled by the underlying disordered configuration. Our study elucidates the crucial role of geometric constraints on the dynamics that has two distinct regimes in terms of target perimeter P_0 . The extended RFOT theory provides a number of testable predictions that we verify in our simulations. The unusual sub-Arrhenius relaxation results from the distinct type of interaction potential arising from the perimeter constraint in a regime controlled by geometric restriction. Fragility of the system decreases with increasing P_0 in the experimentally relevant low- P_0 regime, whereas the dynamics is independent of P_0 in the other regime.

Hallmarks of glassiness in collective motion of cells [1–3] are important for many biological processes such as morphogenesis [4–7], wound healing [8–11], vertebrate body axis elongation [12], tumor progression [6, 13], bronchial asthma [14, 15] etc. Developing a detailed theoretical framework for the glassy dynamics in such systems is, therefore, an important task. Inspired by the physics of soap bubbles, vertex-based models [16–20] that represent individual cells by polygons have provided important insights into the dynamics of epithelial monolayers [21–26]. The cellular perimeter within these models are somewhat abstract and by construction straight or has a constant curvature between vertices whereas it can arbitrarily deviate from a straight line in experiments [19, 27]. How this deviation affects the dynamics remains unknown. Moreover, T_1 transitions, that is crucial for dynamics in such systems, needs to be externally imposed, whose detailed nature remains unclear [15].

Another important class of models is the cellular Potts model (CPM) [28–30] that has been used for modeling cellular dynamics in a variety of scenarios like single and collective cellular behavior [31–34], cell sorting [28, 29], dynamics on patterned surfaces [35], gradient sensing [35, 36] etc. The primary difference between CPM and vertex-based models is the details of energy minimization [37]. Two crucial aspects of CPM, however, makes it advantageous over vertex-based models. First, it allows simulation of actual cell perimeters, and second, T_1 transitions are naturally included within CPM where dynamics takes place at a temperature T . Despite its widespread applicability, glassiness within CPM remains relatively unexplored. To the best of our knowledge, there exists only one such simulation study [38],

which did not consider the perimeter constraint and, as we show below, models with and without this constraint are qualitatively different. Our focus in this work is the equilibrium system. Although biological systems are inherently out of equilibrium and activity is crucial, it is important to first understand the behavior of an equilibrium system in the absence of activity, which can then be easily included [39].

Simulation studies of vertex-based models have established a rigidity transition at a critical value of the input shape index [14, 23]. It has been argued that this rigidity transition controls the glassy dynamics in such systems and the observed shape index has been interpreted as a static order parameter of glass transition [23, 24]. We show that such an interpretation is incorrect. The dynamics within vertex and voronoi models have been shown to be similar and no rigidity transition was found in the latter [26, 40]. Moreover, the glassy dynamics in monodisperse and bidisperse voronoi models have been shown to be similar. Combining numerical studies of a more microscopic CPM for a confluent monolayer and analytical theory based on random first order transition (RFOT) theory of glasses, we clarify these confusing findings. Our aim in this work is twofold, first, we bridge the gap in numerical results through detailed Monte-Carlo (MC) based simulation study of CPM in the glassy regime, second, we develop RFOT theory [41, 42] for a confluent system in glassy regime and show that glassiness in such systems is controlled by the underlying disordered configurations. The main results of this work are as follows: (i) target area does not affect the dynamics in a confluent system, (ii) target perimeter, P_0 , that parameterizes the interaction potential, plays the role of a control parameter, (iii) dynamics at low- P_0 and large- P_0 regimes are different due to geometric restrictions that manifests in the form of a rigidity transition, (iv) change in fragility as well as the unusual sub-Arrhenius relaxation in such systems are results of the perimeter con-

^{*}Electronic address: ssadhukhan@tifrh.res.in

[†]Electronic address: saroj@tifrh.res.in

straint.

I. RESULTS

Incompressibility of cells in 3D [43] and the experimental findings of almost constant height of a monolayer [21] allows a 2D description of the system with an area constraint. On the other hand, mechanical properties of a cell is mostly governed by cellular cortex [43] that can be encoded in a perimeter constraint. Intercellular interactions through different junction proteins like E-Cadherins and effects of pressure, contractility, cell adhesion etc are included within an effective interaction term [21]. Then the energy function for CPM corresponding to a confluent monolayer [30, 37] becomes

$$\mathcal{H} = \lambda_A \sum_{i=1}^N (A_i - A_0)^2 + \lambda_P \sum_{i=1}^N (P_i - P_0)^2 + J \sum_{\langle ij \rangle} (1 - \delta_{\sigma_i, \sigma_j}) \quad (1)$$

where N is the total number of cells in the system, A_i and P_i are area and perimeter of the i th cell, A_0 and P_0 are target area and target perimeter, chosen to be same for all the cells. λ_A and λ_P are elastic constants related to area and perimeter constraints. $\delta_{\sigma_i, \sigma_j}$ is Kronecker delta function which is unity when $\sigma_i = \sigma_j$ and zero otherwise. Note that the third term containing J above is proportional to P_i and can be included within the λ_P term (SM Sec. IA), however, for the ease of discussion we choose to keep this term separately. Dynamics within such monolayers proceeds via active nonequilibrium processes like cell juncture remodeling and employment of a myriad of proteins. Within CPM, such processes are simply represented through an effective temperature T [28, 30]. We perform extensive Monte-Carlo (MC) simulations for the dynamics at T via an algorithm [44] that allows us to locally calculate the perimeter and makes it possible to simulate large system sizes for long times appropriate to investigate glassy dynamics. Fragmentation of cells is forbidden [45] in our simulation to minimize noise and make the results comparable to simulation studies of vertex-based models [23, 24, 26]. We mainly focus on the model with $J = 0$ and get back to the model with $J \neq 0$ and $\lambda_P = 0$, that was simulated in Ref. [38], towards the end of this section.

Dynamics is independent of A_0 : The change in energy coming from the area term alone for an MC attempt $\sigma_i \rightarrow \sigma_j$ between i th and j th cells (SM Sec. IC) is $\Delta\mathcal{H}_{area} = 2\lambda_A(1 - A_i + A_j)$ that is independent of A_0 . Since A_0 dependence of dynamics can only come through $\Delta\mathcal{H}_{area}$, the dynamics becomes independent of A_0 . This result is a consequence of the energy function, Eq. (1), and the constraint of confluency. For a polydisperse system, A_0 , determines average cell area, but, again, does not affect the dynamics directly (SM, Sec (IC)). The input shape index, $s_0 = P_0/\sqrt{A_0}$, therefore cannot be a control parameter for the dynamics in a confluent system [14, 23, 24, 46, 47] and should be viewed

as a dimensionless perimeter. P_0 on the other hand parameterizes the interaction potential and plays the role of a control parameter. Since dynamics in such a system essentially changes A_i and P_i , even in a monodisperse system in steady state, we typically see a distribution for both A_i and P_i (Fig. 1(a)), implying dispersion of both cell area and interaction. This effectively makes the system akin to a polydisperse system allowing it to avoid the periodic minimum.

Two different regimes of P_0 : The observed shape index, $q = \langle P_i/\sqrt{A_i} \rangle$, where $\langle \dots \rangle$ denotes average over all cells, tends to a constant with decreasing P_0 and has been interpreted as a structural order parameter of glass transition via simulation studies of vertex-based models [14, 23, 24]. However, as we show below, such an interpretation is *incorrect* and the result is simply a consequence of geometric restriction. At high T , where dynamics is fast, irregular cell boundaries leads to larger values of P_i and q . Figure 1(b) shows q at three different T as a function of P_0 ; at a fixed P_0 , q decreases with decreasing T . Perimeter of a cell with a certain area has a minimum value, P_{min} , that depends on geometric constraints, here confluency and underlying lattice. When P_0 is below P_{min} , P_i of most cells can not satisfy the perimeter constraint in Eq. (1) as they remain stuck around P_{min} . When dynamics is really slow as in the glassy regime, lowest value of q is dictated by this geometric restriction in the low- P_0 regime. Our interpretation is consistent with the fact that q in a large class of distinctly different systems has similar value [48].

On the other hand, when $P_0 > P_{min}$, the large- P_0 regime, most cells are able to satisfy the perimeter constraint and the lowest value of q is governed by P_0 . To prove this, we show q at T_g as a function of P_0 in Fig. 1(c); it shows saturation of q in the low- P_0 regime whereas it increases linearly with P_0 in the large- P_0 regime. The geometric restriction is also evident from the plot of $\langle P_i \rangle - P_0$ as a function of P_0 ; it decreases linearly with increasing P_0 in the low- P_0 regime and then tends to zero. The interfacial tension, defined as $\gamma = \partial\mathcal{H}/\partial P_i \propto (P_i - P_0)$ [32], is non-zero along cell boundaries in the low- P_0 regime and becomes zero as P_0 increases. Thus, the rigidity transition found in vertex models [14, 23] is essentially a manifestation of this geometric restriction, which is also evident in the inherent structure of the system.

The inherent structure energy, E_{IS} , (SM, Sec. (II)) characterizes the metastable local minima that are quantified through the configurational entropy, s_c , although the exact relation among them remains unknown [49]. Since A_0 does not affect the dynamics, we set it to the average area such that E_{IS} , coming from the area term in Eq. (1), is zero for a cell with average area. E_{IS} is non-zero in the low- P_0 regime and zero in the large- P_0 regime where each of the cells satisfies the constraints. $E_{IS}(P_0)$, the ensemble averaged E_{IS} , strongly depends on P_0 in the low- P_0 regime and then becomes zero (Fig. 1d). In the low- P_0 regime, a broad distribution of E_{IS} , as shown

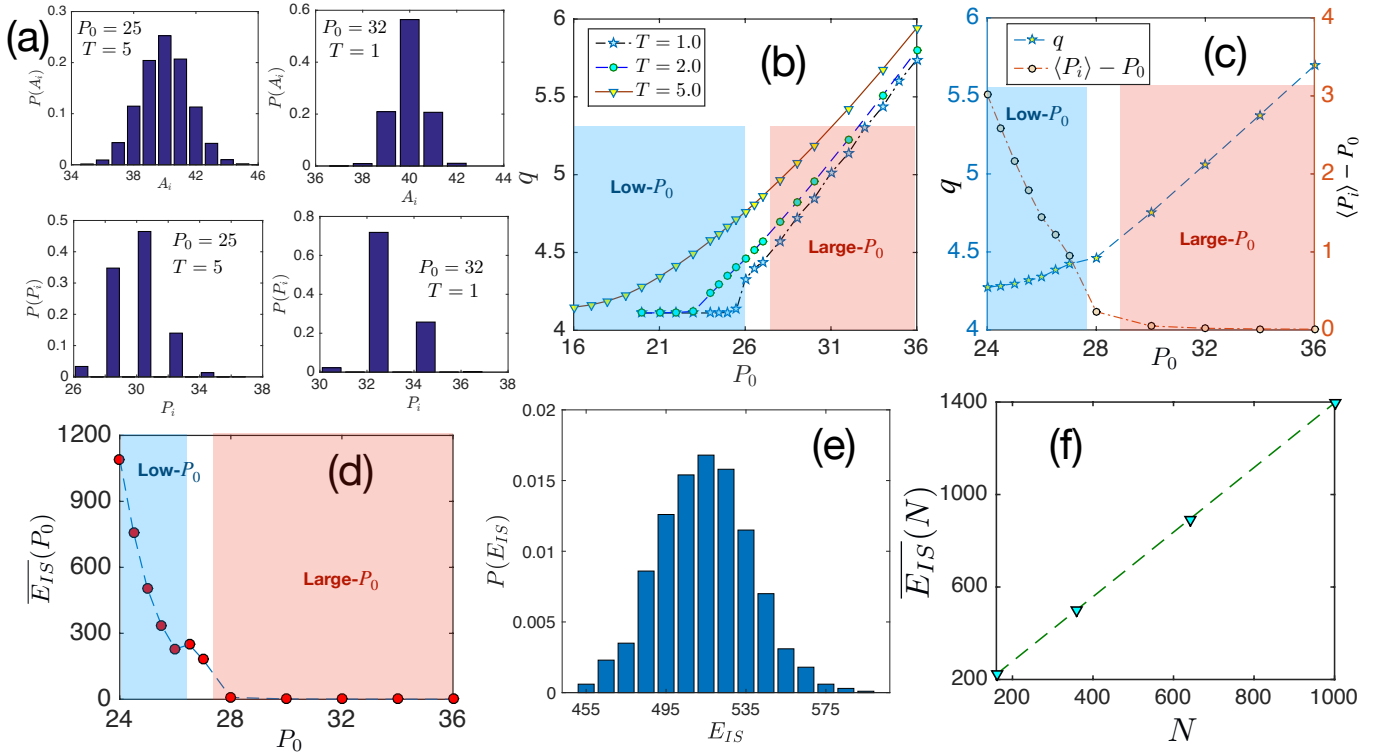


FIG. 1: Nature of steady state and inherent structure in cellular Potts model. (a) A monodisperse system in steady state has a distribution of A_i and P_i as shown for two different P_0 and T values quoted in the figures. This effectively leads to a polydisperse system. (b) Observed shape index, q , as a function of P_0 at three different T ; $P_{min} = 26$ in our simulations (see Appendix). Lowest value of q is given by geometric restriction in the low- P_0 regime and by P_0 in the large- P_0 regime. (c) q at T_g as a function P_0 tends to saturate at low- P_0 regime and increases linearly with P_0 in the large- P_0 regime. Right y -axis shows $\langle P_i \rangle - P_0$ decreases linearly with increasing P_0 in the low- P_0 regime and then tends to zero. Each point in (b) and (c) is an average over $10^5 t_0$. (d) Average inherent structure energy, \overline{E}_{IS} shows strong dependence on P_0 in the low- P_0 regime and then it becomes zero. (e) Broad distribution of inherent structure energy E_{IS} in the low P_0 regime is consistent with the existence of many local minima. $P_0 = 25$ and initial equilibration $T = 4.0$ for this figure. (f) Linear dependence of \overline{E}_{IS} on system size, N , suggests extensivity of configurational entropy. Each point in (d) and (f) is an average over at least 10^3 ensembles.

in Fig. 1(e), is consistent with the existence of many local minima configurations and a linear variation of \overline{E}_{IS} as a function of cell number, N , (Fig. 1(f)) shows \overline{E}_{IS} , and hence s_c , is extensive. Although E_{IS} is zero in the large- P_0 regime, the inherent structure is disordered (SM Fig. 6) and there exist a large number of minima separated by varying energy barriers. These results suggest the existence of glassy dynamics and the applicability of RFOT theory phenomenology in both regimes. If rigidity transition controls the dynamics, as argued in [23, 24], one does not expect glass transition in the large- P_0 regime. But, as we show, the system does show glassiness even in this regime and this is consistent with the RFOT phenomenology where glassiness comes from the underlying disordered configurations.

RFOT theory for CPM: Within RFOT theory, a glassy system consists of mosaics of different states (SM, Sec. III). The typical length scale, ξ , of such mosaics is determined from the balance of two competing contributions; first, the configurational entropy, s_c , that facilitates escape of a mosaic to a different state and thus

reduces ξ , second, the surface reconfiguration energy, Γ , that accounts for energy cost at the surface of two different states and thus, increases ξ [41, 42, 50, 51]. Minimizing the free energy cost for escaping the state of a certain region, one obtains $\xi \sim (\Gamma/s_c)^{1/(d-\theta)}$ where d is the dimension and θ is the exponent relating surface area and length scale of a region. The target perimeter P_0 sets the inter-cellular interaction potential within CPM, and therefore, s_c and Γ are functions of P_0 as they both stem from this potential. Considering linear T -dependence of Γ [52], we write $\Gamma = \Xi(P_0)T$. The relaxation dynamics within RFOT theory is governed by relaxation of these mosaics of typical length scale ξ . We now consider an Arrhenius-type argument where the energy barrier for relaxation of a region of length scale ξ varies as $\sim \xi^\psi$. Taking the exponents as $\theta = \psi = d/2$ [42, 52, 53], we obtain the relaxation time τ (SM Sec. III) as

$$\ln \left(\frac{\tau}{\tau_0} \right) = \frac{E\Xi(P_0)}{s_c(P_0)}, \quad (2)$$

where E is a constant and τ_0 is a high- T timescale that

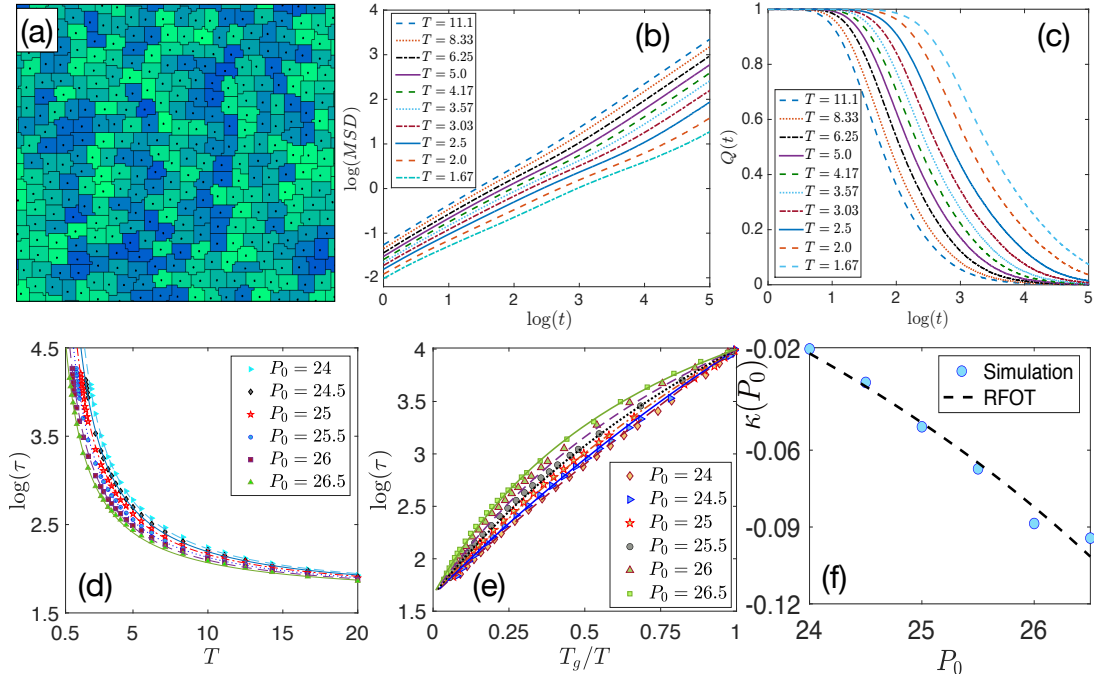


FIG. 2: Behavior of CPM in the low- P_0 regime. (a) Typical configuration of a system at $P_0 = 25$ and $T = 2.5$, close to T_g . Due to the underlying lattice structure, minimum perimeter configuration for a certain area is a square that shows up in the low T configuration. (b) Mean square displacement (MSD) and (c) self-overlap function, $Q(t)$, as a function of time t for $P_0 = 25$ shows typical glassy behavior where growth of MSD and decay of $Q(t)$ becomes slower with decreasing T . (d) Relaxation time τ as a function of T for different P_0 , symbols are simulation data and lines are the corresponding RFOT theory plots (Eq. 5). (e) Angell plot in this regime shows sub-Arrhenius relaxation, symbols are data and lines are RFOT theory predictions. (f) Simulation data (symbols) for kinetic fragility, $\kappa(P_0)$, in this regime also agrees well with the RFOT theory prediction (line).

can depend on interatomic interactions and, hence, P_0 . The theory presented here is somewhat similar in spirit with the RFOT theory for network materials obtained by Wang and Wolynes [54]. Eq. (2) gives the general form of RFOT theory for the CPM and we are going to obtain the detailed forms for $\Xi(P_0)$ and $s_c(P_0)$ for different systems and regimes that we consider below.

Low P_0 regime: As discussed above, P_i for most cells are less than P_0 in this regime. We show a typical configuration of cells as well as their centers of mass in Fig. 2(a) for $P_0 = 25$ and $T = 2.5$, close to T_g . The mean-square displacement (MSD) and the self-overlap function $Q(t)$ (defined in the Appendix) as a function of time t show typical glassy behavior (Figs. 2b,c). We define relaxation time, τ , as $Q(t = \tau) = 0.3$. For a particular P_0 , the glass transition temperature, T_g , is defined as $\tau(T_g) = 10^4$.

We now develop the RFOT theory for CPM in this regime. Our approach is perturbative in nature where we treat a confluent system consisting of particles that want to minimize area and perimeter as a reference system around which we are going to expand the effect of P_0 . The perimeter constraint in the form of P_0 is written as some interaction potential $\Phi(P_0)$ and $\Phi(0)$ gives the reference system potential. Then $s_c[\Phi(P_0)]$ can be

written as

$$s_c[\Phi(P_0)] = s_c[\Phi(0)] + \left. \frac{\delta s_c[\Phi(P_0)]}{\delta \Phi(P_0)} \right|_{P_0=0} \delta \Phi(P_0) + \dots, \quad (3)$$

where $\delta s_c / \delta \Phi(P_0)|_{P_0=0} \equiv \bar{\kappa}_c$ is a constant and $\delta \Phi(P_0) = c_1 P_0$, where c_1 is a constant. For the reference system, $s_c[\Phi(0)] \sim (T - T_K)$, where T_K is the Kauzmann temperature [41, 42, 52, 55], and therefore, for CPM, we obtain $s_c = (T - T_K + \kappa_c P_0)$ where $\kappa_c = \bar{\kappa}_c c_1$. Similarly, for the surface reconfiguration energy, we can write

$$\Xi[\Phi(P_0)] = \Xi[\Phi(0)] + \left. \frac{\delta \Xi[\Phi(P_0)]}{\delta \Phi(P_0)} \right|_{P_0=0} \delta \Phi(P_0) + \dots, \quad (4)$$

where $\delta \Xi[\Phi(P_0)] / \delta \Phi(P_0)|_{P_0=0} \equiv -\kappa_s / c_1$ is constant. As P_0 increases, the interaction potential decreases allowing more number of different configurations available to the system and makes it easier for reconfiguration, this increases s_c and reduces Ξ respectively, explaining the opposite signs chosen for κ_c and κ_s in the expansions, Eqs. (3) and (4). Writing $E\Xi[\Phi(0)] \equiv k_1$ and $E\kappa_s \equiv k_2$, we obtain from Eq. (2) the RFOT theory expression for τ as

$$\ln \left(\frac{\tau}{\tau_0} \right) = \frac{k_1 - k_2 P_0}{T - T_K + \kappa_c P_0}. \quad (5)$$

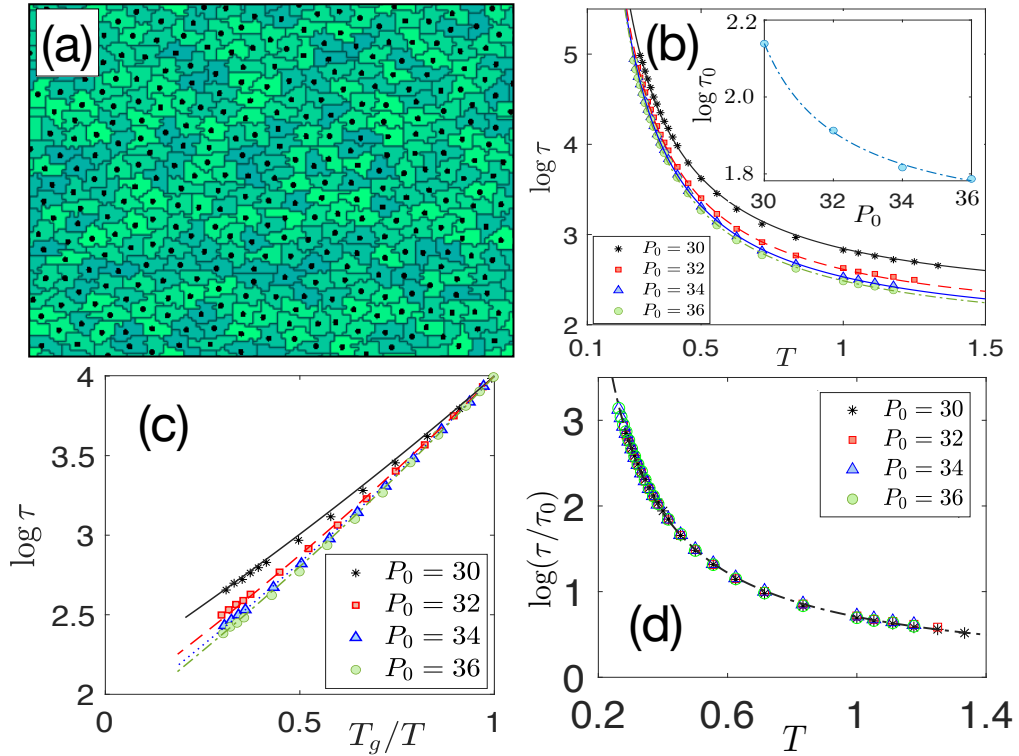


FIG. 3: Behavior of CPM in the large- P_0 regime. (a) Typical configuration of the system with $P_0 = 34$ and $T = 0.5$ close to T_g . The cell boundary assumes a fractal-like nature to satisfy the perimeter constraint and the configuration is disordered. (b) Relaxation time τ as a function of T , symbols are data and lines are RFOT theory fits. **Inset:** τ_0 as a function of P_0 . The line is a fit with a function $\tau_0(P_0) = a + b/(P_0 - c)$ with $a = 3.79$, $b = 2.58$ and $c = 27.72$. (c) Angell plot for the same data (symbols) as in (b), lines are RFOT theory plots (Eq. 6). (d) τ/τ_0 for different P_0 follows a master curve, the line is RFOT theory result. This data collapse shows that glassiness in this regime is independent of P_0 .

The constants k_1 , k_2 , T_K and \varkappa_c are independent of T and P_0 ; they only depend on microscopic details of a system and dimension. For a given system, we treat these constants as fitting parameters in the theory and obtain their values from fit with simulation data. Note that τ_0 depends on the high T properties of the system, which is quite nontrivial and will be explored elsewhere. From our analysis we find that P_0 -dependence of τ_0 is weaker in the low- P_0 regime. Since we are interested in the glassy dynamics here, for simplicity, we take τ_0 to be constant in this regime.

The minimum possible perimeter in our simulation is 26 (see Appendix) and we expect the critical P_0 separating the two regimes to be somewhere between 27 and 28. We first concentrate on the results for $P_0 = 24$ to 26.5 as this is, possibly, the most relevant regime experimentally and present τ as a function of T for different P_0 in Fig. 2(d). We fit one set of data presented in Fig. 2(d) with Eq. (5) and obtain the parameters as follows: $\tau_0 = 45.13$, $k_1 = 42.64$, $k_2 = 1.21$, $T_K = 7.08$ and $\varkappa_c = 0.31$. Note that with these constants fixed, there is no other fitting parameter in the theory, we now show the plot of Eq. (2), as a function of T for different values of P_0 with lines in the same Fig. 2(d) for comparison on top of the simulation data (symbols) for τ . Figure 2(e) shows the

same data in Angell plot representation that shows τ as a function of T_g/T in semi-log scale. All the curves meet at $T = T_g$ due to the definition of T_g . The simulation data agrees well with RFOT predictions in the low T regime where the theory is applicable.

One striking feature of the Angell plot in Fig. 2(e) is the sub-Arrhenius nature of τ whereas it is super-Arrhenius in most glassy systems. Similar results were reported for voronoi model in Ref. [26] demonstrating similarities between CPM and vertex-based models. Within our RFOT theory, the sub-Arrhenius relaxation appears due to the somewhat distinct interaction potential imposed by the perimeter constraint. The regime is essentially controlled by geometric restriction and appears when the system is about to satisfy the perimeter constraint. An important characteristic of this regime is that $(T_K - \varkappa_c P_0)$ becomes negative. We get back to this point later in the paper when we subject our RFOT theory to more stringent tests.

One can define a kinetic fragility, $\kappa(P_0)$ by fitting the simulation data for different P_0 with the form $\ln(\tau/\tau_0) = 1/(\kappa(P_0)[T/T_K^{eff} - 1])$. We present $\kappa(P_0)$ in Fig. 2(f) where symbols are values obtained from fits with simulation data and the dotted line is theoretical prediction, the agreement, again, is remarkable. Fragility of the sys-

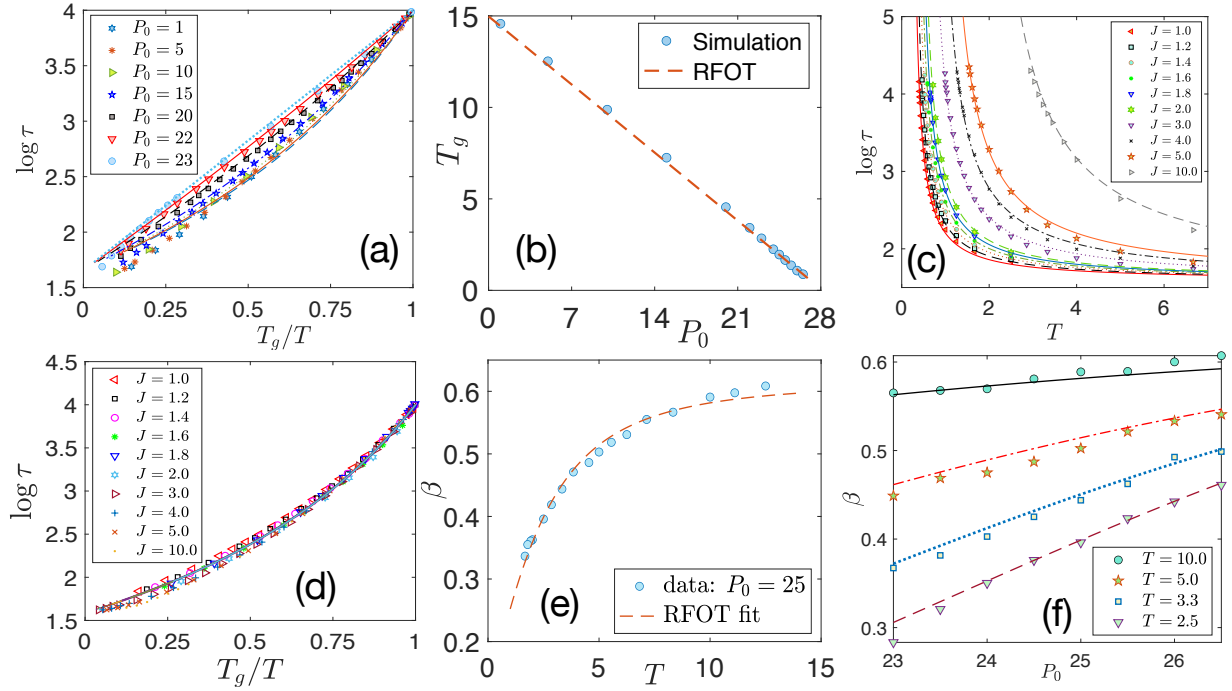


FIG. 4: Tests of our extended RFOT theory. (a) Theory predicts super-Arrhenius behavior for $P_0 \leq 23$. Angell plot for the low- P_0 simulation data (symbols) is consistent with this prediction and τ agrees well with the RFOT theory results, Eq. (5) (lines). (b) Comparison of T_g at different P_0 between simulation data (symbols) and RFOT theory (dashed line). (c) τ for the model with $\lambda_P = 0$ and different values of J , symbols are simulation data and lines are RFOT theory (SM Eq. 18). (d) Our theory predicts super-Arrhenius behavior and no change in fragility when $\lambda_P = 0$, this is well-supported by simulation data (symbols) that follow a master curve in the Angell plot representation, the lines are RFOT theory plots. (e) Stretching exponent β for $P_0 = 25$ as a function of T . Fit of simulation data with the RFOT theory expression, Eq. (7), gives $\mathcal{A} = 0.62$ and $\mathcal{B} = 0.3$. (f) The trend of β as a function of P_0 at different T agrees well with the RFOT theory prediction, Eq. (7), with \mathcal{A} and \mathcal{B} obtained from the fit shown in (e).

tem decreases as P_0 increases and $\kappa(P_0)$ becomes more negative consistent with stronger sub-Arrhenius behavior.

Large- P_0 regime: Cell boundary in this regime becomes fractal-like as P_0 increases as shown in Fig. 3(a) for $P_0 = 34$ close to T_g . Most cells satisfy the perimeter constraint in this regime and the dynamics becomes independent of P_0 implying constant values of Ξ and s_c . Then the RFOT theory in this regime becomes

$$\ln\left(\frac{\tau}{\tau_0(P_0)}\right) = \frac{\Xi}{T - T_K}, \quad (6)$$

where any P_0 -dependence in the dynamics must essentially come from τ_0 implying we can not neglect P_0 -dependence of τ_0 .

Figure 3(b) shows τ as a function of T ; they clearly vary for different P_0 . We now fit Eq. (6) to one set of data and obtain $\Xi = 1.54$, $T_K = 0.052$ and a corresponding value for $\tau_0(P_0)$. Keeping Ξ and T_K fixed, we next fit rest of the data to obtain $\tau_0(P_0)$. The fits are shown by the lines in Fig. 3(b) and $\tau_0(P_0)$ is shown in the inset where the line is a proposed form for $\tau_0(P_0) \sim 1/(P_0 - \text{constant})$. Figure 3(c) shows the Angell plot representation of the same data as in (b) and the corresponding RFOT theory

plots are shown by lines. Figure 3(d) shows τ/τ_0 as a function of T for different values of P_0 , all the data following a master curve supports our hypothesis that the P_0 -dependence in this regime comes from $\tau_0(P_0)$. This also signifies the importance of understanding the high T behavior of the system and will be taken up in a separate work. More importantly, if the rigidity transition controls the glassiness in the system, one would expect no glassy behavior in this regime. However, our simulation results show the presence of glassy behavior even in this regime and the existence of disordered configurations imply it is also expected within RFOT theory that agrees well with the simulation results. q at T_g in this regime is proportional to P_0 as shown in Fig. 1(c), thus, q cannot be the order parameter for the glass transition.

Further tests for extended RFOT theory: Having demonstrated that our RFOT theory captures the key characteristics of glassiness in a confluent system with the energy function given by Eq. (1), we now subject our theory to more stringent tests through three different questions as described below.

Within the theory sub-Arrhenius behavior is found when P_0 contribution to s_c , i.e., $\kappa_c P_0$, becomes larger than T_K (Eq. (5)). This implies super-Arrhenius behav-

ior for $P_0 \leq T_K/\kappa_c \sim 23$. We now simulate the system in this regime and show the Angell plot in Fig. 4(a) where the symbols represent simulation data and the corresponding lines are the RFOT theory predictions. We emphasize that these curves are not fits, we simply plot Eq. (5) with the constants as obtained earlier. All the relaxation curves for different P_0 are super-Arrhenius in nature as predicted by the theory. We also show the comparison of T_g , obtained from simulation and the RFOT predictions, for different P_0 in Fig. 4(b).

Next, our RFOT theory traces the sub-Arrhenius behavior and negative kinetic fragility to the perimeter constraint in Eq. (1). Hence, if we set $\lambda_P = 0$ and look at the glassy behavior as a function of J (Eq. 1), the system should not only show super-Arrhenius behavior, the fragility should be constant (i.e., Angell plot representation of τ should follow a master curve). We show the simulation data for τ as a function of T for different J in Fig. 4(c) (symbols) and the corresponding RFOT theory (SM, Eq. 18) predictions (lines). The Angell plot corresponding to these data are shown in Fig. 4(d). Indeed, we find that this system exhibits super-Arrhenius relaxation and the data for different J follow a master curve, in agreement with RFOT theory. These results are important from at least two aspects: first, it shows the predictive power of the theory and it is possible to understand glassiness in such systems from an extended RFOT framework, second, that a system with the perimeter constraint, Eq. (1), is qualitatively different from a system without this constraint.

Finally, we compare the stretching exponent β [56, 57] that describes decay of the overlap function $Q(t) \sim \exp[-(t/\tau)^\beta]$. The RFOT expression (SM, Sec. IV) is

$$\beta = \mathcal{A} \left[1 + \left\{ \frac{\mathcal{B}(k_1 - k_2 P_0)}{T - T_K + \kappa_c P_0} \right\}^2 \right]^{-1/2}, \quad (7)$$

where \mathcal{A} and \mathcal{B} are two constants; we fit Eq. (7) with the simulation data for $P_0 = 25$, as shown in Fig. 4(e), and obtain $\mathcal{A} = 0.62$ and $\mathcal{B} = 0.3$. We then compare the RFOT predictions with simulation data for different P_0 as shown in Fig. 4(f) for four different T . Again, the trends for β agree quite well with theoretical predictions. The remarkable agreements with simulation data shows that our theory captures the key characteristics of glassiness in such systems.

II. DISCUSSION AND CONCLUSION

We have demonstrated that CPM, being more microscopic in nature, can provide crucial insights into the glassiness of a confluent system. However, presence of microstructure within CPM means the quantitative values of the parameters depend on the lattice. For example, the square lattice in our simulation implies the polygon with minimum perimeter for a certain area is a square.

Moreover, cell perimeter in our system can only have even values due to the discrete lattice, this implies a residual energy for odd values of P_0 although the qualitative results remain similar. The results for odd P_0 are presented in the SM (Sec. V). We find that a voronoi tessellation of cell centers in our simulation underestimates the perimeter (SM, Sec. IX). Qualitative similarities of the results presented here with those from vertex-based simulations [23, 26] seem to suggest glassiness in such systems depend on two key elements, first, the energy function, and second, the confluent nature, and *not* the microscopic details, of the model. Control parameters of glassiness in a confluent system is different from that in particulate systems. The experiments of Ref. [11] on human mammary epithelial MCF-10A cells show that expression of RAB5A, that does not affect number density, fluidizes the system. Careful measurements reveal RAB5A affects the junction proteins in cortex that determine the target perimeter P_0 [11, 58], which is a control parameter for glassiness in such systems.

The observed shape index, q , has been interpreted as a structural order parameter for glassiness in confluent systems via simulation studies of vertex-based models [14, 24]. From theoretical perspective, such a result is quite exciting even if applicable for a certain class of systems alone. However, our analysis shows that such an interpretation is *incorrect* and the value of q in the low- P_0 regime is governed by geometric restriction, which also manifests in the form of the rigidity transition [23]. Our simulation results of glassiness in the large- P_0 regime shows that this rigidity transition can not control the glassiness in such systems, contrary to what has been argued based on vertex-model simulation results [23, 24]. We show through an extended RFOT theory that glassiness in such systems is controlled by the underlying disordered configuration. For example, most cell perimeters in the large- P_0 regime will be tension free, yet their disordered configuration implies a glass transition at low enough T , as found in our simulation and consistent with RFOT theory.

Complete confluency imposes a strong geometric restriction. The main difference between the low- P_0 and the large- P_0 regimes comes from geometric constraint, i.e., the ability of cells to satisfy the perimeter constraint. Our theory traces the unusual sub-Arrhenius behavior to the distinct nature of interaction potential resulting via the perimeter constraint and shows up in a regime where the system is about to satisfy this constraint. The three predictions of the theory that we have discussed, namely super-Arrhenius behavior in a different region of low- P_0 regime, super-Arrhenius and constant fragility in a model with $\lambda_P = 0$ and the stretching exponents at different P_0 agree well with simulation data. These predictions can be easily tested in vertex-based simulations [26], such results will further establish the similarity (or the lack of it) of such models with CPM.

We have shown that the dynamics in a confluent system is independent of target area A_0 . However, it does

have a meaning for the statics of the system [46, 59]; in a polydisperse system $\{A_{0i}\}$ determines average cell areas that can be used to obtain a non-dimensional form for the energy function. We chose *not* to present our results in dimensionless form as it obscures some of the microscopic features of the model and as we wanted to highlight the role of the perimeter. We emphasize here the contrasting roles of A_0 and P_0 , while the former is simply a geometric number the latter parameterizes the interaction potential, then it is not surprising that P_0 is a control parameter in such systems. The lowest value of q when the dynamics is very slow, on the other hand, is simply a geometric effect and should be similar in a large class of systems [48].

Apart from biological importance, we believe, CPM provides an interesting system to study from purely theoretical point of view. It is important to understand how crucial is the constraint of confluency for such behavior, is it possible to devise model systems with curated interaction potential for point particles and still see similar behavior? In any case, the simplicity of CPM allows an opportunity to understand the glassy dynamics in new lights.

III. APPENDIX

Cellular Potts Model: Cellular Potts model on a square lattice in spatial dimension $D = 2$ is defined as follows: each sites on the lattice are associated with a Potts variable $\{\sigma_i = 1, 2, \dots, N\}$ for N distinct cells. The set of sites, with identical Potts variable defines a cell in this model. The dimension of the lattice is $L \times L$ and the unit of length is set by the lattice spacing. Fragmentation of cells is allowed within CPM, however, to reduce fluctuation due to fragmentation, and to make our results comparable to vertex-based models, we impose a condition such that cells remain simply connected at all times [45]. The energy function for the system is given by Eq. (1). The details of the Monte Carlo dynamics at temperature T is as follows: we randomly chose one of the sites i that belongs to cell σ_i and then randomly chose one of its neighbor sites j with cell type σ_j . The dynamics proceeds only if $\sigma_i \neq \sigma_j$, where we attempt to replace σ_i by σ_j with the following rules. We first check if such a move retains local connectivity [45] and then evaluate the change in energy $\Delta\mathcal{H}$ if such a move is accepted. We then accept the move with a probability $\min(1, \exp(-\Delta\mathcal{H}/T))$, note that we have set the Boltzmann constant to unity. Unless otherwise specified, we use a system size of 120×120 with 360 cells and an average cell area of 40. The minimum possible perimeter for a cell with area 40 on a square lattice is 26. Data for different system sizes and cell areas are presented in the SM. We start with a rectangular cell initialization with 5×8 sites having same Potts variable and equilibrate the

system for 8×10^5 MC time steps before the acquisition of data. We have set $\lambda_A = 1$ and the results presented in the main text are for $\lambda_P = 0.5$, other values of λ_P are presented in the SM.

Mean square displacement and self-overlap function: The dynamics is quantified through the mean square displacement (MSD) and the self-overlap function, $Q(t)$. MSD is defined as

$$MSD = \frac{1}{N} \sum_{\sigma=1}^N \overline{\langle (\mathbf{X}_{cm}^{\sigma}(t+t_0) - \mathbf{X}_{cm}^{\sigma}(t_0))^2 \rangle_{t_0}}, \quad (8)$$

where $\mathbf{X}_{cm}^{\sigma}(t)$ is the center of mass of cell σ at time t , $\langle \dots \rangle_{t_0}$ denotes averaging over initial times t_0 and the overline implies an averaging over ensembles. Unless otherwise stated, we have taken 50 t_0 averaging and 20 configurations for ensemble averaging. $Q(t)$ is defined as

$$Q(t) = \frac{1}{N} \sum_{\sigma=1}^N \overline{\langle W(a - |\mathbf{X}_{cm}^{\sigma}(t+t_0) - \mathbf{X}_{cm}^{\sigma}(t_0)|) \rangle_{t_0}}, \quad (9)$$

where $W(x)$ is a heaviside step function

$$W(x) = \begin{cases} 1 & \text{if } x \geq 0 \\ 0 & \text{if } x < 0 \end{cases} \quad (10)$$

and a is a parameter that we set to 1.12.

Inherent Structure energy E_{IS} : Within the inherent structure phenomenology, a certain number of local potential energy minima are available to the system at a particular T . Therefore, equilibrating the system at a certain temperature implies the dynamics is governed by those set of minima accessible at that T . Now setting $T = 0$ and minimizing the energy reveals nature of the energy landscape corresponding to the equilibration temperature as the system gets trapped in those minima. Energy of this minimized state is E_{IS} which depends on the rate of taking $T = 0$, as slower rate takes the system to deeper minima.

For the results shown in Figs. 1(e) and (f) we have equilibrated the system at $T = 4.0$ and reduced T to zero at steps of 0.5 every 2000 MC time. We have checked that slower rates produce lower and higher rates give larger $\overline{E_{IS}}$ (data not shown).

IV. ACKNOWLEDGEMENTS

We would like to thank Mustansir Barma, Chandan Dasgupta, Kabir Ramola, Navdeep Rana, Kallol Paul and Pankaj Popli for many important and enlightening discussions. This project was funded by intramural funds at TIFR Hyderabad from the Department of Atomic Energy (DAE), Government of India.

- [1] T. E. Angelini, E. Hannezo, X. Trepát, M. Marquez, J. J. Fredberg, and D. A. Weitz, *Proc. Natl. Acad. Sci. (USA)* **108**, 4714 (2011).
- [2] S. Garcia, E. Hannezo, J. Elgeti, J. F. Joanny, P. Silberzan, and N. S. Gov, *Proc. Natl. Acad. Sci. (USA)* **112**, 15314 (2015).
- [3] J.-A. Park, L. Atia, J. A. Mitchel, J. J. Fredberg, and J. P. Butler, *J. Cell Sci.* **129**, 3375 (2016).
- [4] D. T. Tambe, C. C. Hardin, T. E. Angelini, K. Rajendran, C. Y. Park, X. Serra-Picamal, E. H. Zhou, M. H. Zaman, J. P. Butler, D. A. Weitz, J. J. Fredberg, and X. Trepát, *Nature Mater* **10**, 469 (2011).
- [5] P. Friedl and D. Gilmour, *Nat. Rev. Mol. Cell Biol.* **10**, 445 (2009).
- [6] A. N. Malmi-Kakkada, X. Li, H. S. Samanta, S. Sinha, and D. Thirumalai, *Phys. Rev. X* **8**, 021025 (2018).
- [7] E.-M. Schötz, M. Lanio, J. A. Talbot, and M. L. Manning, *J. Roy. Soc. Interface* **10**, 20130726 (2013).
- [8] M. Poujade, E. Grasland-Mongrain, A. Hertzog, J. Jouanneau, P. Chavrier, B. Ladoux, A. Buguin, and P. Silberzan, *Proc. Natl. Acad. Sci. (USA)* **104**, 15988 (2007).
- [9] T. Das, K. Safferling, S. Rausch, N. Grabe, H. Boehm, and J. P. Spatz, *Nat. Cell Biol.* **17**, 276 (2015).
- [10] A. Brugués, E. Anon, V. Conte, J. H. Veldhuis, M. Gupta, J. Colombelli, J. J. Muñoz, G. W. Brodland, B. Ladoux, and X. Trepát, *Nat. Phys.* **10**, 683 (2014).
- [11] C. Malinverno, S. Corallino, F. Giavazzi, M. Bergert, Q. Li, M. Leoni, A. Disanza, E. Frittoli, A. Oldani, E. Martini, T. Lendenmann, G. Deflorian, G. V. Bezoussenko, D. Poulikakos, K. H. Ong, M. Uroz, X. Trepát, D. Parazzoli, P. Maiuri, W. Yu, A. Ferrari, R. Cerbino, and G. Scita, *Nat. Mat.* **16**, 587 (2017).
- [12] A. Mongera, P. rowghanian, H. J. Gustafson, elijah Shelton, D. A. Kealhofer, emmet K. Carn, F. Serwane, A. A. Lucio, J. Giammona, and O. Campás, *Nature* **561**, 401 (2018).
- [13] K.-J. Streitberger, L. Lilaj, F. Schrank, a. K.-T. H. Jürgen Braun, M. Reiss-Zimmermann, J. A. Käs, and I. Sack, *Proc. Natl. Acad. Sci. (USA)* **117**, 128 (2020).
- [14] J.-A. Park, J. H. Kim, D. Bi, J. A. Mitchel, N. T. Qazvini, K. Tantisira, C. Y. Park, M. McGill, S.-H. Kim, B. Gweon, J. Notbohm, R. S. Jr, S. Burger, S. H. Randall, A. T. Kho, D. T. Tambe, C. Hardin, S. A. Shore, E. Israel, D. A. Weitz, D. J. Tschumperlin, E. P. Henske, S. T. Weiss, M. L. Manning, J. P. Butler, J. M. Drazen, and J. J. Fredberg, *Nat. Mat.* **14**, 1040 (2015).
- [15] A. Das, S. Sastry, and D. Bi, *bioRxiv* (2020), 10.1101/2020.02.28.970541.
- [16] H. Honda, *J. Theor. Biol.* **72**, 523 (1978).
- [17] H. Honda and G. Eguchi, *J. Theor. Biol.* **84**, 575 (1980).
- [18] M. Marder, *Phys. Rev. A* **36**, 438(R) (1987).
- [19] M. Bock, A. K. Tyagi, J.-U. Kreft, and W. Alt, *Bulletin Math. Biol.* **72**, 1696 (2010).
- [20] S. Henkes, K. Kostanjevec, J. M. Collinson, R. Sknepnek, and E. Bertin, *Nat. Comm.* **11**, 1405 (2020).
- [21] R. Farhadifar, J.-C. Röper, B. Aigouy, S. Eaton, and F. Jülicher, *Curr. Biol.* **17**, 2095 (2007).
- [22] A. G. Fletcher, M. Osterfeld, R. E. Baker, and S. Y. Shvartsman, *Biophys. J.* **106**, 2291 (2014).
- [23] D. Bi, J. H. Lopez, J. M. Schwarz, and M. L. Manning, *Nat. Phys.* **11**, 1074 (2015).
- [24] D. Bi, X. Yang, M. C. Marchetti, and M. L. Manning, *Phys. Rev. X* **6**, 021011 (2016).
- [25] D. L. Barton, S. Henkes, C. J. Weijer, and R. Sknepnek, *Plos Comput. Biol.* **13**, e1005569 (2017).
- [26] D. M. Sussman, M. Paoluzzi, M. C. Marchetti, and M. L. Manning, *Europhys. Lett.* **121**, 36001 (2018).
- [27] J. A. Mitchel, A. Das, M. J. O’Sullivan, I. T. Stancil, S. J. DeCamp, S. Koehler, J. P. Butler, J. J. Fredberg, M. A. Nieto, D. Bi, and J.-A. Park, *bioArxiv* (2020), 10.1101/665018.
- [28] F. Graner and J. A. Glazier, *Phys. Rev. Lett.* **69**, 2013 (1992).
- [29] J. A. Glazier and F. Graner, *Phys. Rev. E* **47**, 2128 (1993).
- [30] T. Hirashima, E. G. Rens, and R. M. H. Merks, *Develop. Growth Differ.* **59**, 329 (2017).
- [31] A. Czirók, K. Varga, E. Méhes, and A. Szabó, *New J. Phys.* **15**, 075006 (2013).
- [32] R. Magno, V. A. Grieneisen, and A. F. Marée, *BMC Biophysics* **8**, 8 (2015).
- [33] E. G. Rens and L. Edelstein-Keshet, *PLoS Comp. Biol.* **15**, e1007459 (2019).
- [34] A. J. Kabla, *J. Royal Soc. Interface* **9**, 3268 (2012).
- [35] A. F. M. Marée, V. A. Grieneisen, and P. Hogeweg, “The cellular potts model and biophysical properties of cells, tissues and morphogenesis,” in *Single-Cell-Based Models in Biology and Medicine*, edited by A. R. Anderson, M. A. Chaplain, and K. A. Rejniak (Birkhäuser Verlag, Switzerland, 2007).
- [36] B. A. Camley and W. J. Rappel, *J. Phys. D: Appl. Phys.* **50**, 113002 (2017).
- [37] P. J. Albert and U. S. Schwarz, *Cell Adhesion and Migration* **10**, 1 (2016).
- [38] M. Chiang and D. Marenduzzo, *Europhys. Lett.* **116**, 28009 (2016).
- [39] S. K. Nandi, R. Mandal, P. J. Bhuyan, C. Dasgupta, M. Rao, and N. S. Gov, *Proc. Natl. Acad. Sci. (USA)* **115**, 7688 (2018).
- [40] D. M. Sussman and M. Merkel, *Soft Matter* **14**, 3397 (2018).
- [41] T. Kirkpatrick and D. Thirumalai, *Rev. Mod. Phys.* **87**, 183 (2015).
- [42] V. Lubchenko and P. G. Wolynes, *Annu. Rev. Phys. Chem.* **58**, 235 (2007).
- [43] J. Prost, F. Jülicher, and J. F. Joanny, *Nat. Phys.* **11**, 111 (2015).
- [44] S. Sadhukhan and S. K. Nandi, “Algorithm for perimeter calculation through local moves in cellular potts model,” (to be submitted).
- [45] M. Durand and E. Guesnet, *Comp. Phys. Comm.* **208**, 54 (2016).
- [46] Y.-W. Li and M. P. Ciamarra, *Phys. Rev. Materials* **2**, 045602 (2018).
- [47] M. Czajkowski, D. M. Sussman, M. C. Marchetti, and M. L. Manning, *Soft Matter* **15**, 9133 (2019).
- [48] R. Li, C. Ibar, Z. Zhou, K. D. Irvine, L. Liu, and H. Lin, *arXiv*, 2002.11166 (2020).
- [49] S. Sastry, *J. Phys.: Condens. Matter* **12**, 6515 (2000).
- [50] J. P. Bouchaud and G. Biroli, *J. Chem. Phys.* **121**, 7347 (2004).

- [51] G. Parisi and F. Zamponi, *Rev. Mod. Phys.* **82**, 789 (2010).
- [52] P. G. Wolynes and V. Lubchenko, *Structural Glasses and Supercooled Liquids* (John Wiley and Sons, Inc., Hoboken, New Jersey, 2012).
- [53] T. R. Kirkpatrick, D. Thirumalai, and P. G. Wolynes, *Phys. Rev. A* **40**, 1045 (1989).
- [54] S. Wang and P. G. Wolynes, *J. Chem. Phys.* **138**, 12A521 (2013).
- [55] W. Kauzmann, *Chem. Rev.* **43**, 219 (1948).
- [56] V. Gupta, S. K. Nandi, and M. Barma, *Phys. Rev. E* (2020), (to be published).
- [57] X. Xia and P. G. Wolynes, *Phys. Rev. Lett.* **86**, 5526 (2001).
- [58] A. Palamidessi, C. Malinverno, E. Frittoli, S. Corallino, E. Barbieri, S. Sigismund, G. V. Beznoussenko, E. Martini, M. Garre, I. Ferrara, C. Tripodo, F. Ascione, E. A. Cavalcanti-Adam, Q. Li, P. P. D. Fiore, D. Parazzoli, F. Giavazzi, R. Cerbino, and G. Scita, *Nat. Mat.* **18**, 1252 (2019).
- [59] M. Durand and J. Heu, *Phys. Rev. Lett.* **123**, 188001 (2019).

Supplementary Material

In this Supplementary Material, we provide a brief description of the cellular Potts model, a discussion of the energy function, simulation details, a discussion of the contrasting roles of the target area and the target perimeter and an illustration of a $T1$ transition that is naturally included within the model in Sec. **SI** followed by a detailed discussion on the source of metastability in the model and the nature of dynamics in Sec. **SII**. Sec. **SIII** provides the details of the calculation of our extended random first order transition theory and the details of the calculation of stretching exponent is provided in Sec. **SIV**. Secs. **SV-SVIII** provide results for the dynamics in the large- P_0 regime for odd values of P_0 , dynamics for different values of λ_P , effect of finite system sizes and effect of different cell sizes on the dynamics respectively, followed by a brief discussion on the differences of CPM and vertex-based models in Sec. **SIX**.

SI. CELLULAR POTTS MODEL FOR BIOLOGICAL TISSUES

The cellular Potts model (CPM) is a mathematical, stochastic, computational lattice based model to simulate the behavior of cellular systems [1–3]. This model is also known as “extended large- q Potts model” and the “Glazier-Graner-Hogeweg (GGH) model” [3–5]. CPM can be simulated both for a single cell as well as a collection of cells with or without fluid in any spatial dimension D . It has wide applications in several biological processes, such as embryogenesis [5], cell sorting [3, 4], gradient sensing [2], wound healing [6] etc. Since our interest in this work is the dynamics of a densely packed cellular monolayer, we restrict our discussion in $2D$.

For the CPM in $2D$, we use a square lattice of size $L \times L$ to represent a confluent cell monolayer. Each cell in this lattice consists of a set of lattice sites with same integer Potts spin (σ), also known as cell index, where $\sigma \in [0, N]$, N being total number of cells. $\sigma = 0$ is usually reserved for fluid that is absent in our model. A typical lattice structure of cells in two dimensional CPM is presented in Fig. (S1).

The cells in this model are evolved by stochastically updating one lattice site at a time through Monte Carlo (MC) simulation via an effective energy function \mathcal{H} , given by

$$\begin{aligned} \mathcal{H} &= \mathcal{H}_A + \mathcal{H}_P + \mathcal{H}_J \\ &= \sum_{i=1}^N \left[\lambda_A (A_i - A_0)^2 + \lambda_P (P_i - P_0)^2 \right] + J \sum_{\langle ij \rangle} (1 - \delta_{\sigma_i \sigma_j}), \end{aligned} \quad (\text{S1})$$

where $\langle ij \rangle$ signifies nearest neighbors, A_i and P_i are the area and the perimeter of i^{th} cell in the monolayer. A_0 and P_0 are the target area and the target perimeter of the cells, chosen to be the same for all cells in a monodisperse system. λ_A and λ_P are the elastic constants associated with the area and perimeter constraints respectively. Interaction between two cells σ_i and σ_j is given by the parameter J , chosen to be same for all cells. δ_{ij} is the usual “Kronecker delta function” having the property: $\delta_{ij} = 1$ if $i = j$ and 0 otherwise. δ_{ij} ensures that the contribution due to the third term in Eq. (S1) is zero when the sites are of same types, thus \mathcal{H}_J is proportional to P_i for i^{th} cell. Positive values of J implies inter-cellular repulsion, whereas negative values give attractive interaction.

4	4	4	4	4	7	7	7
4	4	4	4	7	7	7	7
3	3	4	3	7	7	7	7
3	3	3	3	3	7	6	6
1	3	2	2	3	5	5	6
1	1	1	2	2	5	5	6
1	1	1	2	2	5	6	6
1	2	2	2	5	5	6	6

FIG. S1: Cell representation in two dimensional CPM. Each lattice sites with the same cell index (denoted by a number and color) belongs to one cell.

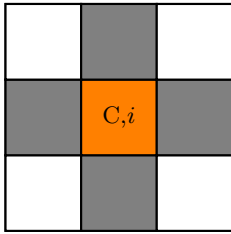


FIG. S2: Von Neumann Neighborhood in CPM: Von Neumann neighbors of the central (C) orange colored cell at site i are the sites in color gray.

A. Inclusion of adhesion term in the perimeter term

The adhesion energy described by \mathcal{H}_J in Eq. (S1) is proportional to the perimeter of the i^{th} cell. So, we can write, $\mathcal{H}_J = \sum_{i=1}^N J P_i$. Therefore, we can rewrite Eq. (S1) as,

$$\mathcal{H} = \sum_{i=1}^N \left[\lambda_A (A_i - A_0)^2 + \lambda_P (P_i - \bar{P}_0)^2 \right] \quad (\text{S2})$$

where $\bar{P}_0 = P_0 - \frac{J}{2\lambda_P}$ is the scaled target perimeter. Note that we have neglected a constant in Eq. (S2) since it does not affect the behavior of the system. For a particular λ_P , dynamics of the system remains unchanged if we vary P_0 and J in such a way that \bar{P}_0 remains same.

In the simulations, we always set $\lambda_A = 1$ and then λ_P and P_0 are the two control parameters. We have explored the dynamics for three different values of λ_P and as a function of P_0 .

B. Simulation Details

Dynamics at a temperature T within CPM proceeds through stochastic attempts to update the cell indices of the lattice sites at each step; unit of time is defined by L^2 attempts of such elemental steps, which are described below.

1. We randomly chose a candidate site i and a target site j from the nearest neighbors of i . Cell indices at i and j are σ_i and σ_j .
2. Dynamics proceeds further only if $\sigma_i \neq \sigma_j$.
3. Check the local connectivity (see below) of the cells if the update is accepted, dynamics proceeds only if local connectivity remains intact.
4. Evaluate the change in energy, $\Delta\mathcal{H}$ if σ_i is updated with σ_j .
5. Accept the move with a probability $\mathcal{P}(\sigma_i \rightarrow \sigma_j) = \min(1, e^{-\Delta\mathcal{H}/T})$, where we have set Boltzmann constant k_B to unity.

During evolution, a site can only be updated with one of its Von Neumann Neighbors (VNN) defined in Fig. S2. If a cell is not locally simply connected, we designate it as a “fragmented cell”. In our simulation, we have followed the “Connectivity Algorithm (CA)” developed by Durand and Guesnet [7] and ensure local connectivity of the cells at all times. Centers of mass of the cells are calculated via the algorithm developed by Bai and Breen [8]. Cell division and apoptosis are forbidden in our simulation as we are interested in the equilibrium properties [9, 10].

For most of the results, we have chosen a square lattice of size 120×120 with 360 total number of cells in the system. Average area of the cells is 40 and the minimum possible perimeter on a square lattice with this area is 26. We have kept $\lambda_A = 1$ fixed and simulated the system for different values of λ_P . $\lambda_P = 0.5$ for the results presented in the main text and other values of λ_P are presented below in Sec. SVI. Note that the dynamics is independent of A_0 in our system, we have simply used A_0 as the average cell area such that the energy contribution from the area term for a cell with average area is zero.

We first equilibrate our system for 8×10^5 MC time steps before the start of collecting data for mean-square displacement (MSD) and self-overlap function, $Q(t)$ (defined in the Appendix). Unless otherwise stated, each of the results is an average over 50 initial times t_0 and 20 ensembles. To test system size effect, we have also studied systems with different simulation box sizes with the largest being 200×200 having 1000 cells with the same cell size as earlier and to observe the finite size effect, we have studied systems with simulation box size 180×180 with cell size 10×9 . For average inherent structure energy calculation, we first equilibrate the system at $T = 4.0$ for 7×10^4 time steps and then decrease T to 0.0 in steps of 0.5 every 2000 time steps; we have also studied other equilibration T , equilibration times and rates to ensure expected behavior. To observe the system size effect in \bar{E}_{IS} , we have taken simulation box of sizes, 200×200 , 160×160 , 120×120 and 80×80 for $P_0 = 25$; for this data, we have used at least 1000 ensembles and larger number of ensembles for smaller systems to ensure good averaging.

The most time consuming part in the simulation is calculation of cellular perimeter at each elemental step. We have developed an algorithm [11] that allows us to locally calculate the perimeter and makes it possible to simulate large system sizes for long times, appropriate to investigate the glassy dynamics.

C. Discussion on A_0 and P_0 in the energy function

We have shown in the main text that the target area in Eq. (S1) does not affect the dynamics, whereas the target perimeter P_0 plays the role of a control parameter. Let us first look at the change in energy, $\Delta\mathcal{H}_{area}$, for $\sigma_i \rightarrow \sigma_j$ in

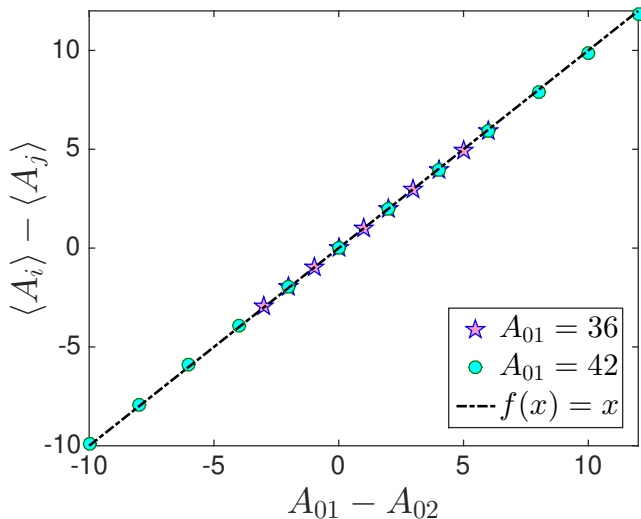


FIG. S3: We have chosen a binary system with different values of target areas. $\langle A_i \rangle$ and $\langle A_j \rangle$ correspond to the average areas of cells with target areas A_{01} and A_{02} respectively. Eq. (S6) predicts $\langle A_i \rangle - \langle A_j \rangle$ should be equal to $(A_{01} - A_{02})$ and this is supported by the simulation data. We have chosen a system of 160 cells with system size 80×80 and each point is averaged over $10^3 t_0$ values.

a monodisperse system coming only from the area term,

$$\begin{aligned} \Delta \mathcal{H}_{area} &= \lambda_A \{ (A_i - 1 - A_0)^2 + (A_j + 1 - A_0)^2 \} \\ &\quad - \lambda_A \{ (A_i - A_0)^2 + (A_j - A_0)^2 \} \\ &= 2\lambda_A(1 - A_i + A_j). \end{aligned} \quad (\text{S3})$$

Thus, $\Delta \mathcal{H}_{area}$ is independent of A_0 for a monodisperse system and thus, A_0 can not affect the dynamics. Let us now consider dispersion of A_0 , and for simplicity, we consider a binary system with two different target areas A_{01} and A_{02} such that their values are consistent with the condition of complete confluency. At equilibrium, individual cells will try to have areas close to their respective target area to minimize energy. At each of the elemental steps, when candidate cell and target cell have same target areas, the situation becomes similar as depicted in Eq. (S3), where A_0 does not affect the dynamics. Let us then examine the case where the two cells have different target areas, A_{01} for the i th cell and A_{02} for the j th cell.

There can be two scenarios in this case, either the target areas are consistent with the condition of complete confluency or they are not. In the first case, average areas of cells will be given by their respective target areas and the individual cell areas can be written as $A_i = A_{01} + \delta A_i$ and $A_j = A_{02} + \delta A_j$, where δA_i and δA_j are fluctuations from their average values. The change in energy coming from the area term for the attempted MC move then becomes

$$\Delta \mathcal{H}_{area} = 2\lambda_A(1 - \delta A_i + \delta A_j), \quad (\text{S4})$$

and thus, independent of A_{01} and A_{02} . On the other hand, when the target areas are not consistent with the

constraint of complete confluency, average area is still set by them. Since each elemental MC step consists of two cells, it suffices to consider a system of two cells, the area part of the energy function is

$$\begin{aligned} \mathcal{H} &= (A_i - A_{01})^2 + (A_j - A_{02})^2 \\ &= (A_i - A_{01})^2 + (A_i - (A_{tot} - A_{02}))^2 \end{aligned} \quad (\text{S5})$$

where $A_{tot} = A_i + A_j$ is the total area. Minimizing Eq. (S5), we obtain the average cell areas as

$$\begin{aligned} \langle A_i \rangle &= A_{01} + \frac{A_{tot} - (A_{01} + A_{02})}{2} \\ \langle A_j \rangle &= A_{02} + \frac{A_{tot} - (A_{01} + A_{02})}{2}. \end{aligned} \quad (\text{S6})$$

Note that the second term in the right hand side in Eq. (S6) above becomes zero when target areas are consistent with constraint of confluency, that is, $(A_{01} + A_{02}) = A_{tot}$. Thus, we expect the difference of average areas of the two cells types to be $A_{01} - A_{02}$ and this agrees with simulation data, as shown in Fig. S3. Going through a similar argument as above, we obtain $\Delta \mathcal{H}_{area}$ to be same as Eq. (S4) in this case as well. This argument can be easily extended for a polydisperse system. Thus, we see that in a confluent monolayer, target area of the cells can not affect the dynamics. Note that $\{A_{0i}\}$, however, has a meaning for the statics of the system. It determines the average cell areas of the different types of cells. Average cell area is a the geometric quantity that determines the critical value of P_0 separating the two regimes in the dynamics.

We now look at the role of P_0 and for this we discuss the perimeter term alone. Let us consider two values of target perimeter, $P_0^{(1)}$ and $P_0^{(2)}$ such that $P_0^{(1)} > P_0^{(2)}$. Then, the perimeter term can be written as

$$\begin{aligned} \lambda_P \sum_{i=1}^N (P_i - P_0^{(2)})^2 &\sim \lambda_P \sum_{i=1}^N (P_i - P_0^{(1)})^2 \\ &\quad + 2\lambda_P (P_0^{(1)} - P_0^{(2)}) \sum_{i=1}^N P_i, \end{aligned} \quad (\text{S7})$$

where we have ignored the constant part. Since $P_0^{(1)} > P_0^{(2)}$, the linear term in the right hand side represents repulsive interaction. This result illustrates that decreasing P_0 results in increased repulsive interaction. This is consistent with the experiments of Park *et al* [12]. Thus, P_0 can be thought of as a parameter of intercellular interaction and hence works as the control parameter for the dynamics. The source of the contrasting roles of A_0 and P_0 is the condition of complete confluency in the system. The change in A_i of the two cells in an elemental MC step must be same to ensure the system remains confluent, whereas that in P_i need not be same and this leads to the distinctly different roles of A_0 and P_0 in such a system.

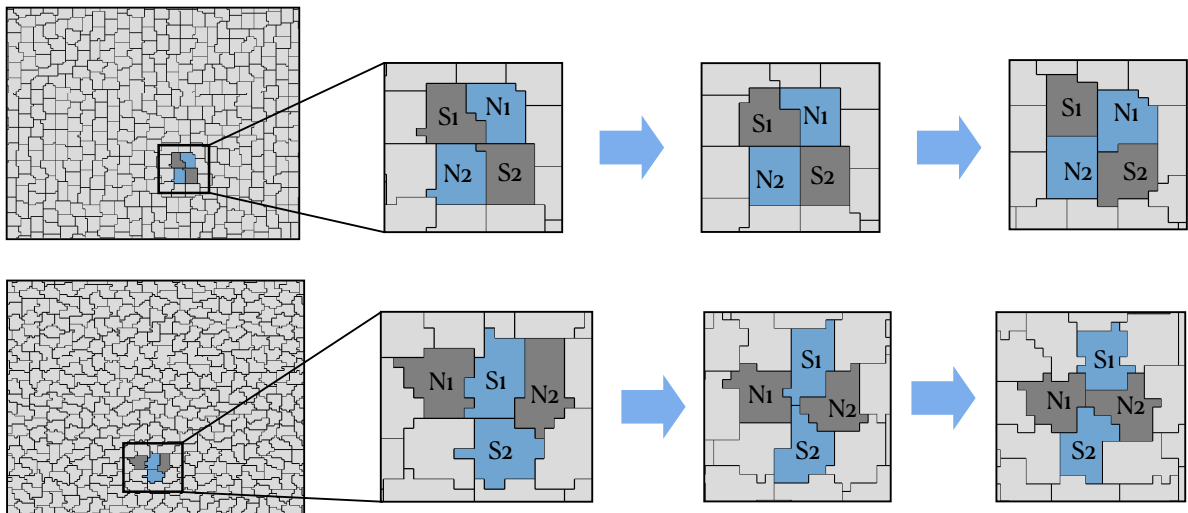


FIG. S4: Snapshots of neighbor exchange or a $T1$ transition process in CPM. Upper panel shows a $T1$ transition event for $P_0 = 25$ at $T = 2.0$ and the lower panel for $P_0 = 32$ at $T = 0.5$; we follow the time evolution of four cells in the system (left most figures) and show the configurations of these cells at three different times. At the first snapshots, S_1 and S_2 share a common boundary whereas N_1 and N_2 don't. The scenario reverses in the third snapshot.

D. $T1$ Transition

Dynamics in a biological tissue proceeds via a series of complicated biochemical processes that are simply represented via an effective temperature T within CPM. At the coarse grained level, an important process for dynamics is known as the $T1$ transition where cells exchange their neighbors [13]. Within vertex-based models, $T1$ transitions need to be carefully implemented with a certain rate. Since $T1$ transitions are the only mode of dynamics, it is then natural that the rate of such transitions is going to crucially affect the dynamics [14]. It remains unclear what controls this rate and how to connect it with different parameters in an equilibrium model, making it difficult for quantitative theoretical development. As discussed in the main text, $T1$ transitions are naturally included within CPM.

In the CPM simulation, as we allow cells to evolve, neighbor exchange and the junctional rearrangements take place via $T1$ transition, where a cell boundary between two cells shrinks to zero and a new cell boundary forms between two other cells that were initially not sharing common boundary. The rate of such transitions within CPM depends on T and P_0 , however, the quantitative details of how this rate compares with the rate in vertex-based models remains an important open question.

We show two such $T1$ transition processes from our simulation in Fig. (S4) for $P_0 = 25$ at $T = 2.0$ (upper panel) and $P_0 = 32$ at $T = 0.5$ (lower panel). In both panels, cells S_1 and S_2 share common boundary in the first snapshot, whereas N_1 and N_2 do not have any common boundary. As time progresses, the boundary be-

tween S_1 and S_2 shrinks (the middle figures) and eventually a common boundary between N_1 and N_2 forms whereas S_1 and S_2 depart from each other (last snapshots in Fig. S4).

SII. SOURCES OF METASTABILITY LEADING TO GLASSY DYNAMICS

It is hard to avoid the crystallization in a monodisperse system of point particles in two dimension, however, as we show below, a two-dimensional monodisperse confluent cellular system is different. The existence of metastability in Potts model in the limit of large Potts variable (> 4) is well-known [15], however, the nature and origin of metastability within CPM remains unclear. Hexagons can entirely tile space in 2D and the constraint of complete confluency makes polygons with six neighbors favorable. However, there are many possible ways to completely tile space with such objects and usually in experiments a distributions of different polygons are found [16]. Glass transition requires disordered metastable configurations and it is crucial to understand the source of this metastability for a complete characterization of the glassy dynamics. We have shown in the main text that even in a monodisperse system, there exists a distribution of A_i and P_i in the steady state effectively leading to a polydisperse system, allowing the system to easily avoid the periodic minimum. Figure S5(a) shows the instantaneous area and perimeter of a particular cell in the steady state. We find that they fluctuate over time and the two do not necessarily follow each other, this is not surprising since it is possible to change one without

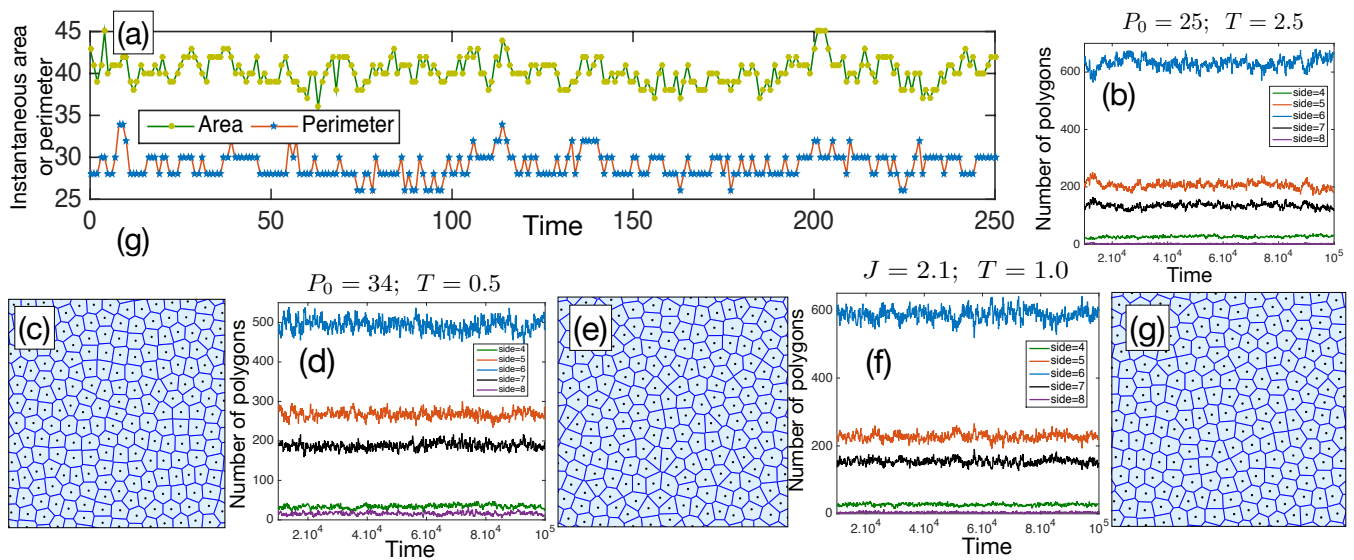


FIG. S5: Instantaneous area and perimeter and distribution of polygons. (a) Variation of instantaneous area and perimeter of a typical cell in the system in steady state with $P_0 = 25$ and $T = 5.0$. Zero of time, noted in the x -axis, is the point when we start collecting data. Note that fluctuation in area is unrelated to that of perimeter (see text). (b-g) Average number of polygons (irrespective of their regularity) in the steady state remains constant over time, signifying the topological disorder does not get annealed out over time. (b) and (d) for systems with $\lambda_P = 0.5$ and values of P_0 and T as noted in the figures, (f) for a system with $\lambda_P = 0$, $J = 2.1$ and $T = 1.0$. (c), (e) and (g) are voronoi tessellations for the centers of mass of the cells in a typical configuration for the systems in (b), (d) and (f) respectively.

changing the other.

Disorder in confluent systems can only be topological in nature. A histogram of polygons (irrespective of their regularity) obtained via voronoi tessellation of centers of mass of the cells reveal largest number of hexagons in steady state as expected for a confluent system and shown in Figs. S5 (b) and (d) for two different values of $P_0 = 25$ and 34 respectively at a T close to their T_g . Figure S5(f) shows similar data for a system with $\lambda_P = 0$ and $J = 2.1$ at $T = 1.0$. Figures S5(c), (e) and (g) shows the voronoi tessellation for centers of mass of a typical configuration of the systems in (b), (d) and (f) respectively. However, Fig. S5 also shows the presence of a significant number of other polygons (mostly with sides 5 and 7) in steady state implying presence of defects leading to disorder and that the system is trapped in a metastable minima.

Key to the random first order transition (RFOT) theory of glassy dynamics is a disordered potential energy landscape with extensive number of minima. As the system explores the energy landscape, it remains stuck in the metastable minima longer as T decreases leading to the slow dynamics. It is imperative to study the nature and existence of metastability in a system to infer applicability of RFOT theory. One straightforward quantity to study in this context is the configurational entropy $s_c = (\log \mathcal{N})/N$, where \mathcal{N} is the number of such metastable minima and N is the number of cells in the system. Known methods of calculating s_c requires complete knowledge of a reference state which is taken as the

high T liquid in particulate systems. However, the high T phase of a confluent system is highly nontrivial and not yet well-understood; thus, the conventional methods are not applicable. We investigate the role of metastability through another related quantity, the inherent structure energy, E_{IS} , although the exact mathematical relation between E_{IS} and s_c is not yet known [17].

Within the inherent structure picture of glassy dynamics, only certain energy minima are accessible to the system at a particular T . If we equilibrate the system at a certain T and then set $T = 0$, the minimized energy, E_{IS} , reflects the accessible energy minima at that T . We have shown in the main text that ensemble averaged inherent structure energy, $\overline{E_{IS}}$, decreases linearly as P_0 increases and then it becomes zero for even values of P_0 . For odd values of P_0 it goes to a different constant due to the residual interaction resulting from the fact that cellular perimeters in our system can only assume even values, however, the qualitative behavior remains same as we show in Fig. S6(a). In the large- P_0 regime, cells are able to satisfy both the area and the perimeter constraints when P_0 is even. When P_0 is odd, they satisfy the area constraint, but the perimeter fluctuates between $P_0 \pm 1$. We typically see a relatively larger number of cells have perimeter $P_0 + 1$, this is expected as there is no restriction on larger perimeter with a certain area¹. Thus, the value

¹ This statement is true for a continuous system. In our lattice

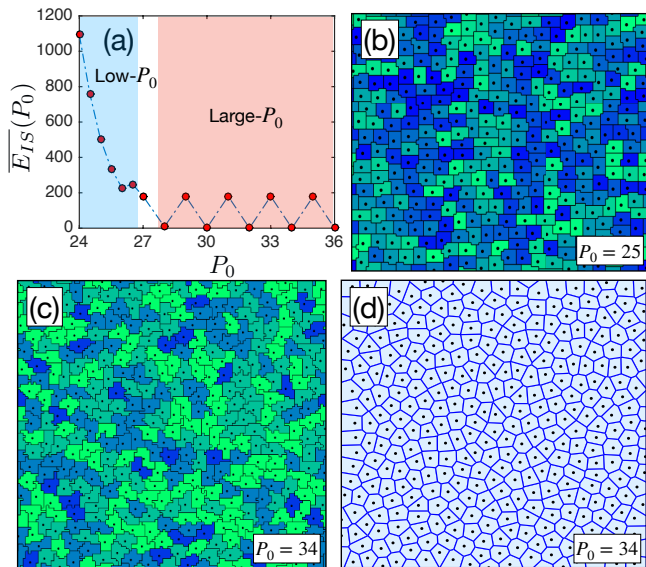


FIG. S6: Inherent structure properties in CPM. (a) The ensemble averaged inherent structure energy, \overline{E}_{IS} , as a function of P_0 has a strong P_0 -dependence in the low- P_0 regime and then saturates to zero for even P_0 and to $\lambda_P N$ for odd P_0 in the large- P_0 regime (see text). (b) Inherent structure configuration for a system with $P_0 = 25$. (c) Inherent structure configuration for a system with $P_0 = 34$ in the large- P_0 regime. Cells in this regime are able to satisfy the area and perimeter constraints when P_0 is even, all the cells in the inherent structure of the system in this regime has average area and target perimeter, 40 and 34 in this case (see text for odd P_0). (d) Voronoi tessellation of the centers of mass of the system shown in (c).

of \overline{E}_{IS} is either zero or $\lambda_P N$ with N being the number of cells as shown in Fig. S6(a).

We show the inherent structure configuration for $P_0 = 25$ in Fig. S6(b) and that for $P_0 = 34$ in Fig. S6(c). We see that the inherent structure configurations are indeed disordered and there exist many different configurations. The energy landscape in the large- P_0 regime looks different from the one in the low- P_0 regime; all the minima are at the same value of energy in the former whereas the energy for different minima are different in the latter. This leads to different behaviors in the two regimes. Note that, although energy of different minima are same in the large- P_0 regime, they are separated by different energy barriers. As T decreases, it becomes difficult for the system to go from one minimum to another leading to the glassy dynamics as characterized in the main text. We also show the voronoi tessellation in Fig. S6(d) of the centers of mass of the inherent structure shown in Fig.

model though, there is an upper limit of $2A_i + 2$, where A_i is the area. Since this upper limit value is very large compared to the regime of our investigation, we expect this upper limit to be irrelevant.

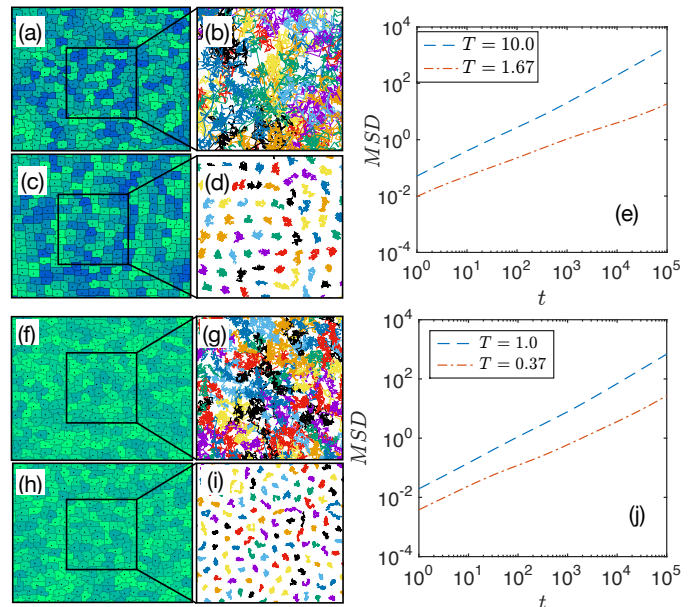


FIG. S7: Qualitative nature of the dynamics. (a) A typical configuration for a system with $P_0 = 25$ and $T = 10$. (b) Trajectories of the centers of mass of the cells inside a region as marked in (a). (c) and (d) are same as in (a) and (b) but at $T = 1.67$, close to the glass transition temperature T_g of the system. (e) Mean square displacement (MSD) of the system at the two different T . (f-j) Same plots as in (a-e) but for $P_0 = 32$, the two different T chosen for these plots are $T = 1.0$ and $T = 0.37$ as shown in (j).

S6(c) to emphasize that the actual perimeter is underestimated by a voronoi tessellation.

A. Qualitative nature of the dynamics

We now briefly discuss the qualitative nature of the dynamics of the system. The system shows glassy behaviors in both low- P_0 and large- P_0 regimes although the behaviors in the two regimes are different. We show typical snapshots of the system for $P_0 = 25$ and $P_0 = 32$ in Fig. S7. We follow the trajectories of the centers of mass of the cells inside the regions marked in Fig. S7. At high T , the cells move quite a lot as revealed by the trajectories of their centers of mass in Figs. S7(b) and (g). As T decreases, the movements become small as seen in the trajectory plots in Figs. S7(d) and (i). The corresponding mean-square displacement (MSD) are shown in Figs. S7(e) and (j) for $P_0 = 25$ and 32 respectively; MSD becomes slower as T decreases, typical of a glassy system. Note the qualitative difference of the cells at low- P_0 and large- P_0 at low T , the cell boundaries are compact in the former (Fig. S7(c)) whereas they become fractal-like in the latter (Fig. S7(h)).

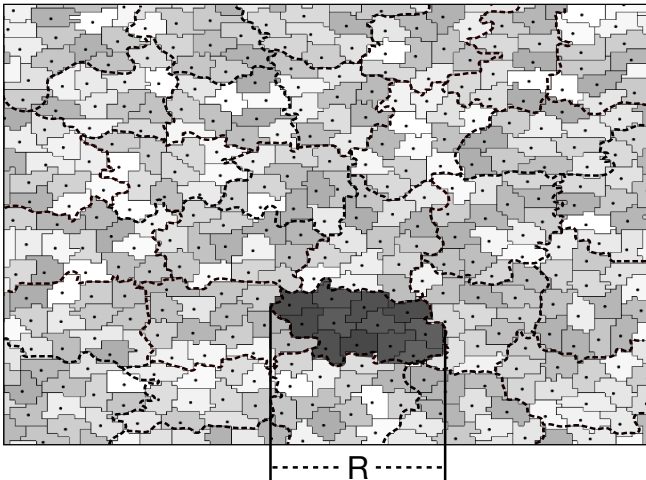


FIG. S8: Schematic representation of the mosaic picture of RFOT theory. A glassy system consists of mosaics of different states as schematically shown by the dashed lines. Typical length scale, ξ , of the mosaics are given by two competing contributions, the configurational entropy and surface reconfiguration energy.

SIII. EXTENDED RANDOM FIRST ORDER TRANSITION THEORY FOR CPM

As shown above as well as in the main text, the CPM has a disordered energy landscape and E_{IS} depends on the target perimeter P_0 . Therefore, we expect random first order transition (RFOT) theory phenomenology should be applicable for the glassy characteristics in such systems. Within RFOT theory, a glassy system consists of mosaics of different states as schematically shown in Fig. S8. Consider a region of length scale R , as shown by the shaded region in Fig. S8, in dimension d and look for the cost in energy for the rearrangement (changing its state) of this region:

$$\Delta F = -f\Omega_d R^d + \Gamma S_d R^\theta, \quad (\text{S8})$$

where f is the decrease in energy per unit volume due to the rearrangement, Ω_d and S_d , volume and surface of a unit sphere, Γ , the surface energy cost per unit surface area due to the rearrangement and $\theta \leq (d-1)$ is the exponent relating surface area and length scale of a region. Within RFOT theory, the drive to reconfiguration is entropic in nature and given by the configurational entropy s_c , that is $f = k_B T s_c$, where k_B is the Boltzmann constant. Minimizing Eq. (S8), we get the typical length scale, ξ , for the mosaics as

$$\xi = \left(\frac{\theta S_d \Gamma}{d \Omega_d k_B T s_c} \right)^{1/(d-\theta)}. \quad (\text{S9})$$

In general, the interaction potential, Φ , of the system determines s_c and Γ . In the case of CPM, the interaction potential is parameterized through P_0 , thus, $\Phi = \Phi(P_0)$.

The temperature dependence of Γ is assumed to be linear [18], thus, $\Gamma = \Xi[\Phi(P_0)]T$ and write Eq. (S9) as

$$\xi = \left(\frac{D \Xi[\Phi(P_0)]}{s_c[\Phi(P_0)]} \right)^{1/(d-\theta)}, \quad (\text{S10})$$

where $D = \theta S_d / d k_B \Omega_d$. Within RFOT theory, relaxation dynamics of the system comes from relaxations of these individual mosaics of typical length scale ξ . The energy barrier associated for relaxation of a region of length scale ξ is $\Delta(\xi) = \Delta_0 \xi^\psi$, where Δ_0 is an energy scale. The relaxation time then becomes $\tau = \tau_0 \exp(\Delta_0 \xi^\psi / k_B T)$, where τ_0 is a microscopic time scale independent of T , but can depend on interatomic interaction potential, hence, on P_0 . Taking $\Delta_0 = \kappa T$, where κ is a constant [19, 20] and setting k_B to unity, we obtain τ as

$$\ln \left(\frac{\tau}{\tau_0} \right) = \kappa \left\{ \frac{D \Xi[\Phi(P_0)]}{s_c[\Phi(P_0)]} \right\}^{\psi/(d-\theta)}. \quad (\text{S11})$$

Following Refs. [20, 21] we take $\theta = \psi = d/2$ and then Eq. (S11) can be written as

$$\ln \left(\frac{\tau}{\tau_0} \right) = \frac{E \Xi[\Phi(P_0)]}{s_c[\Phi(P_0)]}, \quad (\text{S12})$$

where $E = \kappa D$ is another constant. The theory presented here is similar in spirit with that for a network material obtained by Wang and Wolynes [22]. Our approach is perturbative in nature and we look at the effect of P_0 by expanding the potential around a reference system. As discussed in the main text, the behavior of the system are different in the low- P_0 and the large- P_0 regimes that we discuss separately below.

Low- P_0 regime: In this regime cells are not able to satisfy the perimeter constraint and the effect of P_0 on the dynamics is strong. We consider the system with $P_0 = 0$ as our reference system. Therefore, we have

$$\begin{aligned} s_c[\Phi(P_0)] &= s_c[\Phi(0)] + \left. \frac{\delta s_c[\Phi(P_0)]}{\delta \Phi(P_0)} \right|_{P_0=0} \delta \Phi(P_0) + \dots \\ \Xi[\Phi(P_0)] &= \Xi[\Phi(0)] + \left. \frac{\delta \Xi[\Phi(P_0)]}{\delta \Phi(P_0)} \right|_{P_0=0} \delta \Phi(P_0) + \dots \end{aligned} \quad (\text{S13})$$

where we have ignored higher order terms. $s_c[\Phi(0)]$ for the reference system vanishes at Kauzmann temperature T_K , thus,

$$s_c[\Phi(0)] = \Delta C_p (T - T_K) / T_K, \quad (\text{S14})$$

where ΔC_p is difference of specific heat between the liquid and the periodic crystalline phase. It is evident from the discussion in Sec. SIC, $\delta \Phi(P_0)$, the change in potential due to a non-zero P_0 from the state $P_0 = 0$, is proportional to P_0 . Our reference state is a confluent tightly packed state, any non-zero positive P_0 increases repulsive interaction facilitating dynamics. This suggests

higher s_c with increasing P_0 while Ξ decreases. Therefore, we can write the first order terms as

$$\begin{aligned} \left. \frac{\delta s_c[\Phi(P_0)]}{\delta \Phi(P_0)} \right|_{P_0=0} \delta \Phi(P_0) &= \bar{\kappa}_c P_0 \\ \left. \frac{\delta \Xi[\Phi(P_0)]}{\delta \Phi(P_0)} \right|_{P_0=0} \delta \Phi(P_0) &= -\bar{\kappa}_s P_0. \end{aligned} \quad (\text{S15})$$

Using Eqs. (S13-S15) in Eq. (S12), we obtain

$$\ln \left(\frac{\tau}{\tau_0} \right) = \frac{k_1 - k_2 P_0}{T - T_K + \bar{\kappa}_c P_0} \quad (\text{S16})$$

where $k_1 = T_K E \Xi(0) / \Delta C_p$, $k_2 = T_K E \bar{\kappa}_s / \Delta C_p$ and $\bar{\kappa}_c = T_K \bar{\kappa}_c / \Delta C_p$ are all constants. Since the change in potential in the low- P_0 regime remains proportional to P_0 , we expect Eq. (S16) to remain valid in the entire region.

Large- P_0 regime: The individual cells are able to satisfy the perimeter constraint in this regime, hence the actual value of P_0 becomes irrelevant for the glassy dynamics and both s_c and Ξ become independent of P_0 . Therefore, we can simply write the RFOT theory expression for τ in this regime as

$$\ln \left(\frac{\tau}{\tau_0} \right) = \frac{\Xi}{T - T_K}, \quad (\text{S17})$$

where the detailed values of Ξ and T_K for our system depend on whether P_0 is even or odd since P_i can have even values only. Except this difference, the RFOT theory parameters, and hence the glassy dynamics, become independent of P_0 . However, the vestige of P_0 -dependence still remains in the dynamics through the high T properties of the system. We can not ignore the P_0 -dependence of τ_0 in this regime, and, as we show in the main text, the difference in τ for different values of P_0 can be understood in terms of $\tau_0(P_0)$.

System with $\lambda_P = 0$ and non-zero J : This system lacks any particular reference state and this makes the system different from that with $\lambda_P \neq 0$. Perturbative expansion around a state with $J = 0$ is problematic and therefore, we need to chose a system with a moderate value of J . However, then any value of J is as good as any other. One consequence of this is that we expect the fragility of the system to be constant as discussed in the main text. Since the repulsive interaction only comes in the form of J , the trend of variation of s_c and Ξ with increasing J becomes opposite to that in the low- P_0 regime above. Considering the reference system at a moderate value of J , we go through a similar set of arguments and obtain the RFOT expression for τ as

$$\ln \left(\frac{\tau}{\tau_0} \right) = \frac{k_1 + k_2 J}{T - T_K - \bar{\kappa}_c J}, \quad (\text{S18})$$

where k_1 , k_2 , T_K and $\bar{\kappa}_c$ are constants. Note the opposite signs of the constants k_2 and $\bar{\kappa}_c$ in Eq. (S18) and Eq. (S16). Fitting Eq. (S18) with simulation data for $J = 1$,

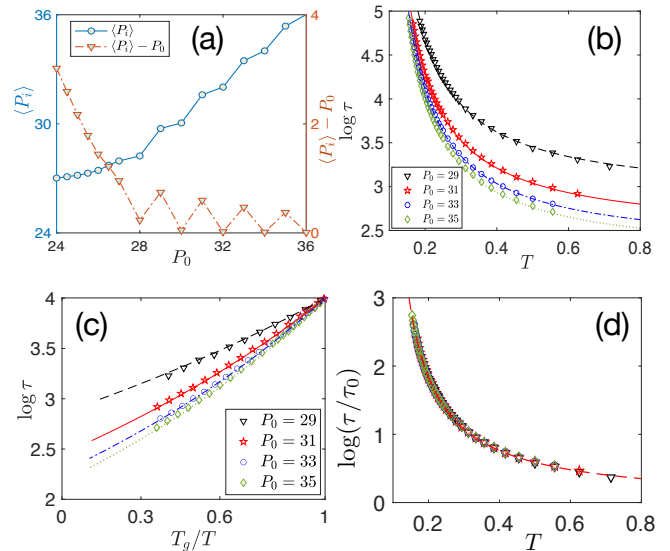


FIG. S9: Behavior of CPM at the large- P_0 regime for odd values of P_0 . (a) $\langle P_i \rangle$ for odd values of P_0 is slightly higher than that for even P_0 . Right y-axis shows $\langle P_i \rangle - P_0$ as a function of P_0 which goes to zero with increasing P_0 with a slower rate than even P_0 . (b) Relaxation time τ as a function of T for odd values of P_0 . These data are well fitted with Eq. (6) in the main text with $\Xi = 0.60$ and $T_K = 0.058$ and $\tau_0(P_0)$ as a fitting parameter. $\tau_0(P_0)$ has a similar behavior (not shown) as for even values of P_0 shown in the inset of Fig. (3b) in the main text. Lines are the RFOT theory fits. (c) τ in the Angell plot representation agrees well with the RFOT theory. (d) Plot of $\tau/\tau_0(P_0)$ as a function of T for different values of P_0 follows a master curve, implying that the glassiness for odd values of P_0 is also independent of P_0 in this regime.

we obtain $k_1 = 0.284$, $k_2 = 0.84$, $T_K = 0.04856$ and $\bar{\kappa}_c = 0.157$. Comparison of Eq. (S18) with the simulation data is presented in the main text, Figs. 4(c) and 4(d).

SIV. STRETCHING EXPONENT FOR THE DECAY OF $Q(t)$

It is well-known that the decay of self-overlap function $Q(t)$ in a glassy system can be described through a stretched exponential function [23], the Kohlrausch-Williams-Watts (KWW) formula [24, 25] given by,

$$Q(t) = A \exp[-(t/\tau)^\beta], \quad (\text{S19})$$

where A is a constant, of the order of unity, τ , the relaxation time and β is the stretching exponent. RFOT theory allows calculation of β through the fluctuation of local free energy barriers ΔF [26]. We assume that ΔF follows a Gaussian distribution given by,

$$P(\Delta F) = \frac{1}{\sqrt{2\pi\sigma_F^2}} \exp \left[-\frac{(\Delta F - \Delta F_0)^2}{2\sigma_F^2} \right] \quad (\text{S20})$$

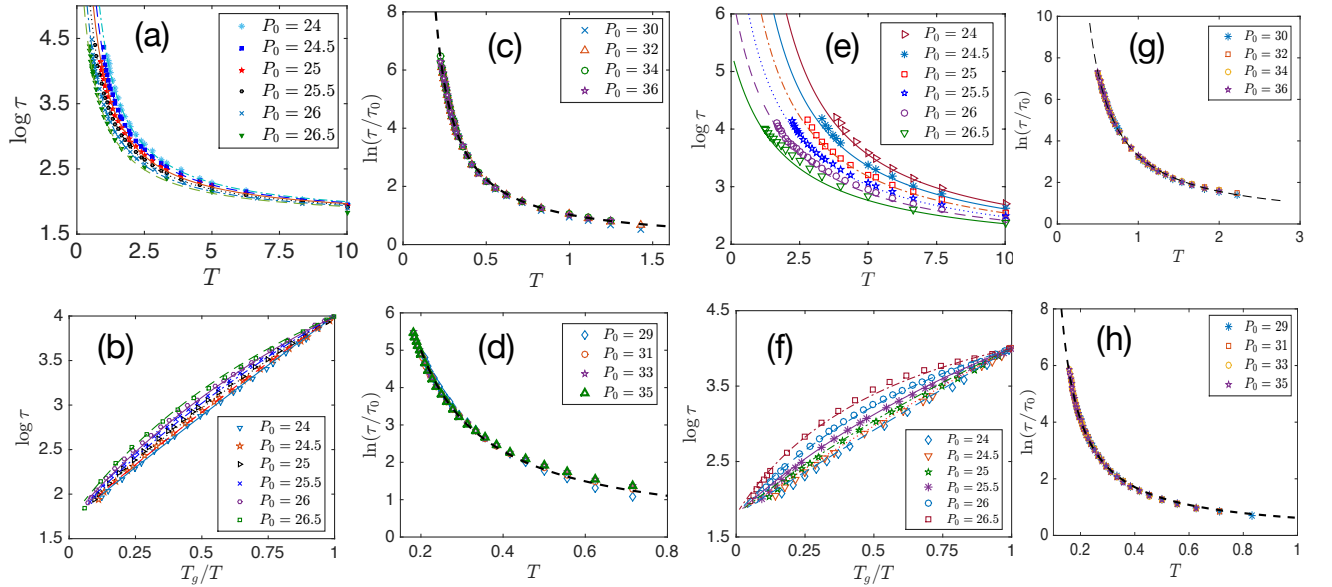


FIG. S10: Results for $\lambda_P = 0.25$ (a-d) and $\lambda_P = 1.0$ (e-h). (a) τ as a function of T for different P_0 with $\lambda_P = 0.25$. Symbols are simulation data and lines are RFOT theory, Eq. (S16), with the constants provided in Table I. (b) Same data as in (a) but shown in the Angell plot representation. (c) τ/τ_0 as a function of T for different values of even P_0 in the large- P_0 regime follow a master curve showing the P_0 -dependence in this regime comes from that in τ_0 . (d) Same as in (c) but for odd values of P_0 . (e-h) Corresponding plots as in (a-d) for $\lambda_P = 1.0$. Qualitative nature of the results shown here are similar with those for $\lambda_P = 0.5$ presented in the main text.

where ΔF_0 is the mean of the distribution and σ_F^2 is the standard deviation, which gives a measure of the fluctuation. Following Xia and Wolynes [26], we obtain β as

$$\beta = \left[1 + \left(\frac{\sigma_F}{T} \right)^2 \right]^{-\frac{1}{2}}, \quad (\text{S21})$$

where we have set Boltzmann constant k_B to unity.

For the Gaussian distribution of ΔF , we obtain [26],

$$\frac{\delta s_c}{\langle s_c \rangle} \sim \frac{\sigma_F}{\Delta F_0}, \quad (\text{S22})$$

with $\delta s_c \sim \sqrt{\Delta C_p/V}$, where $V \sim \xi^d$ is the typical volume of the mosaics. In the low- P_0 regime, where we have compared our RFOT theory predictions with the simulation results, the length scale ξ of the mosaics, Eq. (S9), is given by,

$$\xi \sim \left[\frac{k_1 - k_2 P_0}{T - T_K + \kappa_c P_0} \right]^{1/(d-\theta)} \quad (\text{S23})$$

$$\text{and, } \langle s_c \rangle \sim \frac{\Delta C_p}{T_K} (T - T_K - \kappa_c P_0). \quad (\text{S24})$$

Using Eqs. (S23) and (S24), we obtain

$$\frac{\delta s_c}{\langle s_c \rangle} \propto (k_1 - k_2 P_0)^{-1}. \quad (\text{S25})$$

The mean free energy barrier (ΔF_0) is obtained, by using $R = \xi$ in Eq. (S8), as

$$\Delta F_0 \propto \left[\frac{T(k_1 - k_2 P_0)^2}{T - T_K + \kappa_c P_0} \right]. \quad (\text{S26})$$

Using Eqs. (S25), (S26) and (S22) in Eq. (S21), we obtain β as

$$\beta = \left[1 + \left\{ \frac{\mathcal{B}(k_1 - k_2 P_0)}{T - T_K + \kappa_c P_0} \right\}^2 \right]^{-1/2} \quad (\text{S27})$$

where \mathcal{B} is a constant. It is well-known that RFOT theory predicts the correct trends of β , but the absolute values differ by a constant factor even for a particulate system [26]. Since we are interested in the trend of β as a function of P_0 , we multiply Eq. (S27) by a constant \mathcal{A} to account for this discrepancy and obtain

$$\beta = \mathcal{A} \left[1 + \left\{ \frac{\mathcal{B}(k_1 - k_2 P_0)}{T - T_K + \kappa_c P_0} \right\}^2 \right]^{-1/2}. \quad (\text{S28})$$

The constants k_1 , k_2 , T_K and κ_c are already determined, \mathcal{A} and \mathcal{B} are obtained through the fit of Eq. (S28) with the simulation data for $P_0 = 25$ as a function of T .

The decay of $Q(t)$ at high T is stretched exponential followed by a power law at long times. To avoid this high T power-law regime in the data, we fit the data up to a time τ , that is when $Q(t) = 0.3$ with Eq. (S19) and obtain β as shown in Figs. 4 (e) and (f) in the main text.

SV. DYNAMICS IN THE LARGE- P_0 REGIME FOR ODD VALUES OF P_0

We now present the results for odd values of P_0 in the large- P_0 regime. As stated in the main text, the qualitative behaviors for odd P_0 are similar to those with even P_0 , however, since the cell perimeter can only be even due to the underlying lattice, $\langle P_i \rangle - P_0$ goes to zero with increasing P_0 at a slower rate than that for even P_0 as shown in Fig. S9(a). The data for relaxation time τ as a function of T is shown in Fig. S9(b) by symbols and the corresponding RFOT theory fits of Eq. (6) in the main text are shown by lines with $\Xi = 0.60$ and $T_K = 0.058$; $\tau_0(P_0)$ has a similar behavior as shown in the inset of Fig. (4b) in the main text. The Angell plot representation, as shown in Fig. S9(c) of the same data as presented in Fig. S9(b), agrees well with the RFOT theory. Finally, to show that glassiness in this regime for odd values of P_0 is also independent of P_0 , we plot τ/τ_0 as a function of T and find excellent data collapse for different values of P_0 as shown in Fig. S9(d) and the master curve agrees well with the RFOT theory (line).

SVI. DYNAMICS FOR DIFFERENT λ_P

The qualitative behavior of the system for different values of λ_P remains same, although the quantitative values of different parameters within the RFOT theory description depends on λ_P . For the results presented in the main text, we have used $\lambda_P = 0.5$; here we present the results for $\lambda_P = 0.25$ in Figs. S10 (a-d) and for $\lambda_P = 1.0$ in Figs. S10 (e-h). For the two values of λ_P , we show τ as a function of T in the low- P_0 regime for different P_0 in Figs. S10(a) and (e) and the corresponding Angell plots in Figs. S10(b) and (f); the unusual sub-Arrhenius behavior, found for $\lambda_P = 0.5$ as shown in the main text is also present at these two different values of λ_P . The glassy dynamics becomes independent of P_0 in the large- P_0 regime as confirmed by the data collapse for τ/τ_0 as a function of T , shown in Figs. S10(c) and (d) for even and odd values of P_0 respectively for $\lambda_P = 0.25$ and in Figs. S10(g) and (h) for even and odd values of P_0 respectively for $\lambda_P = 1.0$. This implies any P_0 -dependence in this regime must come from that of $\tau_0(P_0)$. The symbols in Fig. S10 are simulation data and the lines are RFOT theory predictions, Eq. (S16), with the constants given in Table I.

TABLE I: Values of the constants k_1 , k_2 , κ_c and T_K , appearing in Eq. (S16), for different values of λ_P .

λ_P	k_1	k_2	κ_c	T_K
0.25	21.4929	0.610723	0.146849	3.45708
0.5	42.6428	1.21128	0.307531	7.07889
1.0	73.7929	2.21207	0.685	16.3378

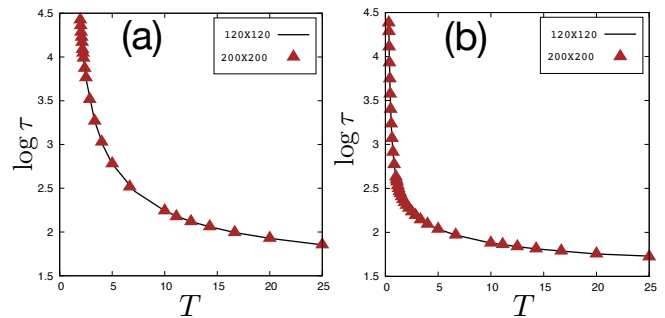


FIG. S11: Finite system size effects are negligible in our results. We plot τ as a function of T for two different systems of sizes 120×120 and 200×200 for $P_0 = 24$ in (a) and $P_0 = 32$ in (b). Data for the two systems overlap. Cell sizes of average area 40 are same in these two systems.

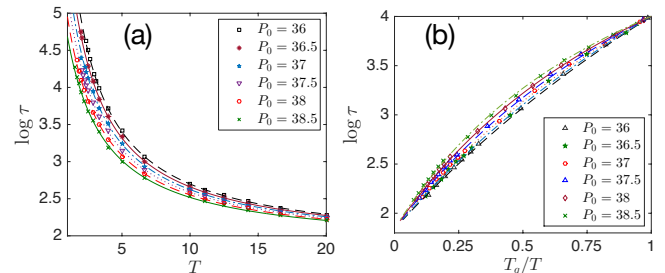


FIG. S12: Systems with varying cell sizes have different average cell areas. This sets the value of P_0 separating the low- P_0 and large- P_0 regimes as it is a geometric effect. Except this, the qualitative behavior of the system remains same as with other cell sizes. (a) τ as a function of T for different P_0 , (b) same data as in (a) in the Angell plot representation. Symbols are simulation data and lines are the RFOT theory, Eq. (S16), with the constants quoted in the text.

SVII. EFFECT OF FINITE SYSTEM SIZES ON THE DYNAMICS

To investigate the effect of finite sizes of the system on the dynamics, we have looked at several systems of different sizes $L \times L$ where L varies from 80 to 200 keeping the sizes of the cells same, i.e., of area 40. We find that the results for the system size 120×120 that we have mainly investigated and presented the results in the main text remain unchanged when we use larger system sizes. For a comparison, we show τ as a function of T for two different systems in Fig. S11 for $P_0 = 24$ and 32, the data for the two systems are essentially same.

SVIII. EFFECT OF DIFFERENT CELL SIZES

We have shown in the main text that the two different regimes result due to geometric constraint where the cells can not fully satisfy the perimeter constraint in the low- P_0 regime whereas they are able to satisfy it in the large-

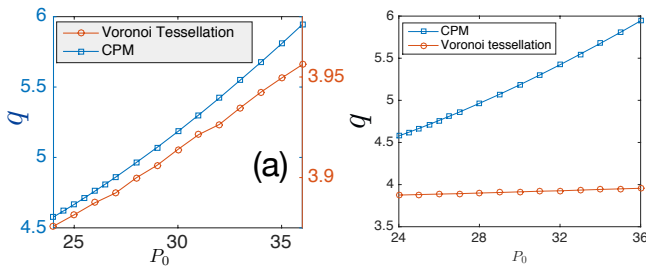


FIG. S13: Observed shape index, $q = \langle P_i/\sqrt{A_i} \rangle$, for the CPM and that obtained via the Voronoi tessellation of the centers of mass of the cells. (a) Two estimates are plotted in two different scales to emphasize their qualitatively similar behavior as a function of P_0 . (b) They are plotted on the same scale to highlight that Voronoi tessellation underestimates the value of q in comparison to its actual value in CPM, the discrepancy becomes larger at higher P_0 .

P_0 regime. As we vary the sizes of cells in the system, numerical value of P_0 representing the transition from one regime to the other changes, but apart from that, the qualitative behavior of the system remains same. We have verified this with different systems of various cell sizes. We present simulation data of τ as a function of T for a system of size 180×180 with average cell area 90 and 360 total number of cells in Fig. S12 (a) and the same data in Angell plot representation in Fig. S12 (b). We have used $\lambda_P = 0.5$ for these simulations to compare the results with those presented in the low- P_0 regime in the main text. For average cell area 90, the minimum possible perimeter is 38, thus, we expect the transition point to be somewhere between 39 and 40. Lines in Fig. S12 represent plots of RFOT theory, Eq. S16, with the parameters as follows: $\tau_0 = 68.72$, $k_1 = 71.9$, $k_2 = 1.39$, $\kappa_c = 0.29$ and $T_K = 9.37$. We have checked (data not presented) that glassiness in the large- P_0 regime becomes independent of P_0 . Thus, the main features of glassiness in this system are similar to those for the system with average cell area 40 as presented in the main text.

SIX. DIFFERENCE OF CPM AND VERTEX-BASED MODELS

CPM and vertex-based models can be viewed as the lattice based model and its continuum version respec-

tively for a confluent cellular system. The qualitative behavior for the results obtained via the two models with the same energy function are expected to be same since the primary difference between the models are how energy is minimized. However, there are a number of differences at the quantitative level.

- CPM, being a lattice based model, the ratio of minimum perimeter to square root of area as well as the shape of this polygon depend on the underlying lattice structure, for example, for the square lattice used in our simulation, these are 4 and a square respectively.
- As shown in Sec. SID, T_1 transitions are naturally included within CPM [3, 4] whereas they need to be externally implemented in vertex-based models with a certain rate [14].
- Shapes of the cellular perimeter can in principle be arbitrary within CPM, whereas it is by construction a straight line between two vertices in the vertex-based models or can at most vary with a certain curvature [6, 27]. We show the observed shape index $q = \langle P_i/\sqrt{A_i} \rangle$ for different values of P_0 at a fixed $T = 5.0$ in Fig. S13 from the two different estimates. First, we obtain the actual values of q in the CPM, second, we construct a Voronoi tessellation for the centers of mass of the cells and obtain q for that system. We find that though the qualitative trends for both estimates are similar, that is they both monotonically increase with P_0 as shown in Fig. S13(a) (note the difference in scales), the Voronoi tessellation underestimates q as shown in Fig. S13(b); the discrepancy becomes higher at larger P_0 where the Voronoi tessellation can not account for nonlinear cell boundaries.

[1] T. Hirashima, E. G. Rens, and R. M. H. Merks, *Develop. Growth Differ.* **59**, 329 (2017).
[2] A. F. M. Marée, V. A. Grieneisen, and P. Hogeweg, “The cellular Potts model and biophysical properties of cells, tissues and morphogenesis,” in *Single-Cell-Based Models in Biology and Medicine*, edited by A. R. Anderson, M. A. Chaplain, and K. A. Rejniak (Birkhäuser Verlag, Switzerland, 2007).

[3] F. Graner and J. A. Glazier, *Phys. Rev. Lett.* **69**, 2033 (1992).
[4] J. A. Glazier and F. Graner, *Phys. Rev. E* **47**, 2128 (1993).
[5] P. Hogeweg, *J. Theor. Biol.* **203**, 317 (2000).
[6] A. Noppe, A. P. Roberts, A. S. Yap, G. A. Gomez, and Z. Neufeld, *Integrative Biol.* **7**, 1253 (2015).
[7] M. Durand and E. Guesnet, *Comp. Phys. Comm.* **208**,

- 54 (2016).
- [8] L. Bai and D. Breen, *Journal of Graphics, GPU, and Game Tools* **13**, 53 (2008).
 - [9] J. Ranft, M. Basan, J. Elgeti, J. F. Joanny, J. Prost, and F. Jülicher, *Proc. Natl. Acad. Sci. (USA)* **107**, 20863 (2010).
 - [10] D. A. Matoz-Fernandez, K. Martens, R. Sknepnek, J. L. Barrat, and S. Henkes, *Soft Matter* **13**, 3205 (2017).
 - [11] S. Sadhukhan and S. K. Nandi, “Algorithm for perimeter calculation through local moves in cellular potts model,” (to be submitted).
 - [12] J.-A. Park, J. H. Kim, D. Bi, J. A. Mitchel, N. T. Qazvini, K. Tantisira, C. Y. Park, M. McGill, S.-H. Kim, B. Gweon, J. Notbohm, R. S. Jr, S. Burger, S. H. Randell, A. T. Kho, D. T. Tambe, C. Hardin, S. A. Shore, E. Israel, D. A. Weitz, D. J. Tschumperlin, E. P. Henske, S. T. Weiss, M. L. Manning, J. P. Butler, J. M. Drazen, and J. J. Fredberg, *Nat. Mat.* **14**, 1040 (2015).
 - [13] A. G. Fletcher, M. Osterfield, R. E. Baker, and S. Y. Shvartsman, *Biophys. J.* **106**, 2291 (2014).
 - [14] A. Das, S. Sastry, and D. Bi, *bioRxiv* (2020), 10.1101/2020.02.28.970541.
 - [15] O. Mazzarisi, F. Corberi, L. F. Cugliandolo, and M. Picco, *J. Stat. Mech.*, 063214 (2020).
 - [16] R. Farhadifar, J.-C. Röper, B. Aigouy, S. Eaton, and F. Jülicher, *Curr. Biol.* **17**, 2095 (2007).
 - [17] S. Sastry, *J. Phys.: Condens. Matter* **12**, 6515 (2000).
 - [18] P. G. Wolynes and V. Lubchenko, *Structural Glasses and Supercooled Liquids* (John Wiley and Sons, Inc., Hoboken, New Jersey, 2012).
 - [19] V. Lubchenko and P. G. Wolynes, *Annu. Rev. Phys. Chem.* **58**, 235 (2007).
 - [20] T. Kirkpatrick and D. Thirumalai, *Rev. Mod. Phys.* **87**, 183 (2015).
 - [21] T. R. Kirkpatrick, D. Thirumalai, and P. G. Wolynes, *Phys. Rev. A* **40**, 1045 (1989).
 - [22] S. Wang and P. G. Wolynes, *J. Chem. Phys.* **138**, 12A521 (2013).
 - [23] V. Gupta, S. K. Nandi, and M. Barma, *Phys. Rev. E* (2020), (to be published).
 - [24] R. Kohlrausch, *Annalen der Physik* **167**, 179 (1854).
 - [25] G. Williams and D. C. Watts, *Trans. Faraday Soc.* **66**, 80 (1970).
 - [26] X. Xia and P. G. Wolynes, *Phys. Rev. Lett.* **86**, 5526 (2001).
 - [27] M. Bock, A. K. Tyagi, J.-U. Kreft, and W. Alt, *Bulletin Math. Biol.* **72**, 1696 (2010).